Detection of Multi-Decadal Oceanic Variability within a Coupled Ensemble Data Assimilation System

S. Zhang*, A. Rosati and M. J. Harrison

Geophysical Fluid Dynamics Laboratory, Princeton University

Princeton, NJ 08542, USA

First version: Start at 25 April 2005

(submitted to JGR)

* *Corresponding author address:* Shaoqing Zhang, GFDL/NOAA, Princeton University, P.O. Box 308, Princeton, NJ 08542, USA. Email: Shaoqing.Zhang@noaa.gov Tel: (609)452-6540 Fax: (609)987-5063

ABSTRACT

Detectability of long time scale variability of oceanic heat content and salinity has been examined by ensemble oceanic data assimilations within a coupled ocean-atmosphere-land-ice system. The ensemble filter solves for a temporally-varying joint probability density function (joint-PDF) of oceanic states, combining the observational PDF and the prior PDF derived from the oceanic GCM of the coupled system. Based on the 20^{th}-century (temperature only) and 21^{st}-century (ARGO temperature and salinity) oceanic observing networks (OONs), a series of perfect-model experiments was performed to examine the impact of temporally-varying radiative forcings, initial conditions (ICs) and OONs. A coupled-model simulation with the 20^{th}-century historical greenhouse gas and natural aerosol (GHGNA) radiative forcings serves as the "truth" from which observations are drawn by the 20^{th}-/21^{st}-century OON.

Results showed both the 20^{th}- and 21^{st}-century OONs provide adequate sampling to capture the basin scale heat content variability. Within a few-decade assimilation period, the adjustment of oceanic states is dominated by data constraint while the use of historical GHGNA records does not have a significant impact on detection skill. Temporally-varying GHGNA forced ICs produce a better detection skill than fixed-year GHGNA controlled ICs due to the relaxed assimilation shocks from the long time model spinup by temporally-varying radiative forcings, especially in deep oceans. In tropical oceans, due to a strong T-S relationship from air-sea interaction, the use of T-S covariances enables the filter to capture the basic features of salinity variations based on in-situ temperature measurements only. Generally, according to the isopycnal nature of water motions, the utilization of T-S covariances in ODA is very important to maintain the physical balance in oceanic states. However, due to the existence of fresh water forcings at high latitudes and the imperfection of the estimated T-S relationship, the salinity observations provided by the ARGO network are significant for global oceanic climate studies. In particular, they play a key role for correctly reconstructing the North Atlantic thermohaline circulation.

1 Introduction

Coupled model's uncertainties, or say, biases, lead to modeled climate drift from reality. Those uncertainties are caused by inadequate measurements of natural and/or anthropogenic forcings and incomplete understanding of their radiative effects, as well as inaccurate numerical implementation of physical processes. Observations on climate variables such as temperature, salinity and currents etc. provide only some samples of climate variations in time and space, which are always sparse and noisy. A more accurate assessment of climate and climate changes can be achieved by combining coupled model dynamics with observational data. We shall refer to this approach as "estimation of climate states."

Coupled data assimilation (CDA) uses the dynamics of a coupled model to extract the information from observations in order to reconstruct the temporal evolution of climate state variables possessing a 3-dimensional structure. The continuous time series of climate variables produced by CDA are the estimate of historical climate variations, and provide the initial conditions for coupled model climate forecasts or called numerical climate prediction. Applications of reconstruction products help further understanding of mechanisms of climate variations, like the impact of anthropogenic and natural forcings on climate changes; as initial conditions of numerical climate prediction, the assimilation products also provides direct economical values for the human activities by initializing coupled models to launch numerical climate prediction.

The accuracy of estimated climate states sensitive to model bias, assimilation methodology and representativeness of an observational network. The CDA system at GFDL (Geophysical Fluid Dynamical Laboratory, NOAA) (Zhang et al. 2007) solves for a temporally-varying joint probability density function (joint-PDF) of climate state variables using an ensemble filter to combine the observational PDF and a prior PDF derived from coupled model dynamics. The system has the ability to mostly maintain both the physical balance between state variables and/or coupled components, and the high order moments of the joint-PDF. This capability renders the system particularly suitable for solving the problem of climate variations in which error structures of flows are highly anisotropic and strongly dependent on seasonal cycle and interannual fluctuations (Zhang et al. 2005; 2007). When a CDA system has been developed, the first concern that needs to be clarified is: how much of signals in climate variations can be detected based on an existing oceanic observing system? As a sequel to the complete evaluation of the CDA system by Zhang et al. (2007), this study focuses on detectability of oceanic variations based on the 20^{th}-century XBT (mainly expendable bathythermograph, also including CTD and others, see section 3.2) and 21^{st}-century ARGO (Array for Real-time Geostrophic Oceanography) networks. This oceanic climate detection process is carried out by the oceanic data assimilation (ODA) component within the CDA system, i.e., the analysed oceanic states are coupled with an atmospheric GCM in which no data constraint is performed.

Figure. 1 uses the North Atlantic (NA) temperature and salinity trends as an example to illustrate what is climate detection. The North Atlantic heat uptake and meridional overturning circulation (MOC) have been studied well in model simulations (Delworth and Greatbatch 2000; Gent and Danabasoglu 2004). It is therefore a good example to demonstrate the climate detection issue that this study tries to address in a perfect model study framework. The left/right panels (ab/cd) of Fig. 1 present variations of monthly mean temperature vs. salinity over the upper (200-1000m) (panels a and c) and lower (1000-5000m) (panels b and d) North Atlantic (20-70^{o}N) in the GFDL IPCC (Intergovernmental Panel on Climate Change) "control"/"20^{th} century historical" run using the GFDL coupled climate model (CM2) (Delworth et al. 2006; Gnanadesikan et al. 2006). Both the control and historical runs start from the same initial conditions, a 300 year spin-up integration initialized from a previous integration (Stouffer et al., 2004). The control run refers to as a 141-year integration with the 1860 fixed-year greenhouse gas and natural aerosol (GHGNA) radiative forcings while the historical run is an integration using the temporally-varying GHGNA radiative forcings during the period from January 1861 to December 2000. Figure 1 shows that after around 40 years (black dots in all panels) the historical run clearly begins to depart from the control run (each color represents a quarter of the 20^{th} century, e.g., the first quarter is cyan, the last quarter is red, and so on) in both upper and lower portions of the North Atlantic Ocean. In particular, it is shown that while the upper ocean temperature and salinity of the control run vary only within a relatively small range, their counterparts in the historical run exhibit a clear warming and salting trend. The interactions between coupling components of CM2 can be schematically demonstrated in Fig. 2. In response to the GHGNA radiative forcings, the atmosphere in the coupled model forms its circulations, which in return provide the sea-surface forcings for the ocean. Ocean establishes its thermohaline structure and circulations as a dynamical response to the surface forcings (momentum/heat/water fluxes, etc.) from atmosphere, land and sea-ice. Reconstructing historical climate variations by data assimilation involves many issues: validation of the assimilation methodology, sampling of the observing system and coupled model bias, etc. The combination of those aspects and the lack of a complete picture of some important large scale oceanic circulations that have a global impact on climate evolution, such as the NA MOC described above make it extremely difficult to understand the reconstructed results. To reduce the complexity, this study excludes the model bias issue by using a perfect model study framework, or called identical twin experiments, in which "observations" are drawn from a model simulation, the prior defined true solution for assimilation, so that the accuracy of reconstructed signals can be verified with the "truth." This serves as a very important first step for estimation of climate phenomena with multi-decadal variability like the NA MOC and their forecast initialization from observed oceanic states.

Now, we can state the climate detection problem illustrated by Fig. 1 as follows: Given an XBT or ARGO network, how much can we retrieve signals of oceanic climate variations by sampling oceanic states in the truth based on either network and starting from arbitrary initial conditions? In order to answer this question, we need to understand:

1) What is the impact of the GHGNA radiative forcings on coupled data assimilation?

2) What is the impact of coupled initial conditions, especially oceanic initial conditions, on assimilation quality?

3) What is the impact of XBT/ARGO oceanic observing network on estimation of oceanic states?

The rest of this paper is organized as follows: Section 2 and 3 describes the methodology, in which section 2 gives the description of the coupled model and the ensemble filter and section 3 describes experimental design including perfect-model "twin" experiment configuration and 4 assimilation experiments. Sections 4 and 5 present and discuss the detection results on oceanic heat content and salinity, focusing on the impact of temporally-varying radiative forcings, initial conditions and oceanic observing networks. The detectability of the thermohaline structure of the NA MOC is particularly analyzed and discussed in section 6. Summary and discussions are given in section 7.

2 Model and coupled assimilation system

2.1 Model: GFDL fully-coupled GCM – CM2

As described in the system design and evaluation of the GFDL coupled data assimilation system (Zhang et al. 2007), the version of the coupled model used here includes a B-grid finite difference atmospheric dynamical core, called CM2.0 (the other using a finite-volume atmospheric dynamical core is called CM2.1). The B-grid atmosphere model AM2p12 (AM2/LM2, GAMDT 2005) has 24 vertical levels and 2.5° longitude by 2° latitude horizontal resolution. The physics package includes a Mellor-Yamada 2.5 dry planetary boundary layer, relaxed Arakawa-Schubert convection and a simple diffusive parameterization of the vertical momentum transport by cumulus convection. The ocean component is the MOM4 configured with 50 vertical levels, in which 22 levels of the top 220 m have 10 m thickness for each, $1^\circ \times 1^\circ$ horizontal resolution telescoping to $1/3^\circ$ meridional spacing near the equator. The model has an explicit free surface with true freshwater flux exchange between the atmosphere and ocean. Parameterized physical processes include k-profile parameterization vertical mixing, neutral physics, a spatially-dependent anisotropic viscosity, a shortwave radiative penetration depth that depends on a prescribed climatological ocean color. Insolation varies diurnally and the wind stress at the ocean surface is computed using the velocity of the wind relative to the surface currents. An efficient time-stepping scheme (Griffies 2005) is employed. More details can be found in Gnanadesikan et al. (2006) and Griffies (2005). The Sea Ice Simulator in the coupled model is a dynamical ice model with three vertical layers (one snow and two ice) and five ice-thickness categories. The elastic-viscous-plastic technique (Hunke and Dukowicz 1997) is used to calculate ice internal stress, and the thermodynamics is a modified Semtner three-layer scheme (Winton 2000). The interactions of these four major model components (ocean/atmosphere/land/sea-ice) in the coupled system are schematically illustrated in Fig. 2 (black arrows represent the exchange fluxes between coupling components).

2.2 CM2's spread and probability distribution's maintenance of oceanic states

The probabilistic nature of the state evolution of a coupled model system is the basis of implementing coupled ensemble data assimilation. An ensemble-based filter uses a Monte Carlo approach to simulate the model-described prior PDF by finite-ensemble model integrations.

It has been asked frequently how many members are appropriate in ensemble-based data assimilation? This is a very complicated question for which there exists no simple answer. For a certain ensemble assimilation algorithm, a large ensemble size used is expected to maximize signal-to-noise ratio of assimilation but it is stronly constrained by the availability of computation resources. Even under a perfect model assumption, the signal-to-noise ratio of assimilation still depends on many other factors such as the temporal and spatial scales that assimilation model can resolve (i.e. the internal variablility of assimilation model), how to maintain the spread of the stochastic dynamical system (e.g. the representativeness of ensemble), and the features of observations (e.g. the representativeness of observations) etc.

In order to illustrate the CM2's stochastic nature and how the oceanic states obtain and maintain their spread in the coupled model, Fig. 3 presents the time mean ensemble spread of atmospheric and oceanic states over the last 10 years of a 25-year integration of CM2 with 1860 fixed-year radiative forcings, starting from initial atmospheric perturbations only. Each solid line represents the departure of an individual ensemble member's atmospheric (upper panel) and oceanic (lower panel) temperature profile from the ensemble mean; dark dotted lines show the vertical variation of the standard deviation of 6 ensemble members; 6-member ensemble integrations are initialized from 6 yearly-separate atmospheric states (including land) one year apart from the same simulation and a common oceanic state (including ice) (i.e. IC_c described in section 3). Due to the strong internal variability (nonlinearity) of atmospheric flows, perturbations in both initial conditions and sea-surface temperatures (SSTs) generated (as a consequence of ocean-atmosphere interaction) maintain the ensemble spread of the atmospheric state. The ensemble spread of oceanic states reflects the sensitivity of the ocean model to the surface forcings provided by the atmosphere. Due to effects of mixing and convection in upper ocean, atmospheric disturbances can easily penetrate the upper ocean layers and alter the thermocline where the largest oceanic spread is found. In fact, the ensemble spread of oceanic temperature near the surface has the same amptitude as the ensemble spread of atmospheric temperature in lower troposphere. Below thermocline, the uncertainty propagates toward deeper ocean on a longer time scale. This kind of uncertainty can reach deeper than 2000 m in regions such as the North Atlantic, where deep convection is active. Nevertheless the global mean spread appears very small at the depth of 2000 m in Fig. 3.

From Fig. 3, we learned that once an initial error occurs in the atmosphere or other coupled model components, the strong internal variability of atmospheric flows and oceanic state's responses to atmospheric forcings will eventually produce inter-ensemble variations of oceanic states through feedbacks between coupled model components. Experiments (e.g., Zhang et al. 2007) show that due to capturing the nature of oceanic states' uncertainty in the coupled model which consists of a course resolution OGCM, this kind of ensemble system is fairly reliable that it can work with a relatively small ensemble size. In addition, covariance filtering, or called covariance localization, and observation smoothing techniques

(Zhang et al. 2005; 2007) also help enhance the signal-to-noise ratio and maintain the ensemble spread of the system when a small ensemble size is used. More test experiments in Zhang et al. (2007) also show that although a small ensemble size (6 members) is used, the coupled ensemble assimilation system is able to provide such a reliable T-S relationship that the multi-variate assimilation scheme (mainly utilizing T-S cross-covariances) dramatically enhances the assimilation's signal-to-noise ratio relative to a univariate scheme. Considering the character of the coupled model ensemble and those practical techniques as well as the computation resource constraint, we continously use 6 members in this and all follow-up studies wherever a "twin" experiment is conducted, while a much larger ensemble size (up to 24 members) for real data assimilation (will be documented in separete reports, also see related discussions in section 7).

2.3 Assimilation scheme: A coupled ensemble filter

Under the framework of a *filtering* theory, the temporal evolution of states in a coupled system can be viewed as a continuous stochastic dynamical process described by a vectorized stochastic differential equation (Jazwinski, 1970) as $d\mathbf{x}_t/dt = \mathbf{f}(\mathbf{x}_t, t) + \mathbf{G}(\mathbf{x}_t, t)\mathbf{w}_t$. Here, $\mathbf{x}_t$ is an n-dimensional vector representing the coupled model state at time t (n is the size of the model state), $\mathbf{f}$ is an n-dimensional vector function, $\mathbf{w}_t$ is a white Gaussian process (uncorrelated in time) of dimension r with mean 0 and covariance matrix $\mathbf{S}(t)$ while $\mathbf{G}$ is an $n \times r$ matrix. The first and second terms on the right hand side in the equation represent respectively the deterministic modeling and uncertainty contributions in a coupled system. In this context, coupled data assimilation (CDA) solves the problem of sampling the probability of the state of a coupled dynamical system given noisy and sparse measurements.

This study addresses how to retrieve the oceanic climate variations by using only an oceanic observing system within the CDA framework. The oceanic data assimilation (ODA) process in the CDA system adjusts directly the oceanic states using observed data in the ocean by an ensemble filter. The ensemble filter solves for a temporally-varying joint probability density function (joint-PDF) of coupled state variables in a straight forward manner, in terms of discrete representation of joint-PDF by finite-size ensemble members. The filtering process combines the PDF of oceanic observations and a prior PDF derived from the dynamically-coupled model, a continuous stochastic dynamical process, described by the vectorized partial differential equation above. This assimilation process is schematically illustrated in Fig. 4, where the filtering process refers to as a linear regression based on error covariances between the analyzed and observed state variables. The details of the filtering algorithm and its implementation into CM2 can be found in Zhang et al. (2007). The coupled ensemble filter has following several advantages over traditional data assimilation approaches, e.g. optimal interpolation (OI), 3-dimensional variational (3DVar) and 4DVar etc., especially for climate detection applications of particular interest to this study:

1) It is convenient to carry out multi-variate data assimilation using cross-covariances between state variables, which are evaluated in a straight forward manner by the ensemble model integrations. The multi-variate assimilation scheme plays a centrally-important role in maintaining the physical balance described by the temperature-salinity (T-S) relationship in ocean.

2) Error covariances used at each analysis step, evaluated instantaneously by a whole ensemble of state variables, are fully flow-dependent and anisotropic. The flow-dependent and anisotropic nature of error statistics allows the assimilation to capture features of local waves and the vertical variation of oceanic circulations (see the bottom panel of Fig. 3).

3) Higher-order moments of the joint-PDF maintained by the ensemble model integrations allow the assimilation to sustain the nonlinearity in the long term evolution of oceanic circulations. One example is the bi-modal feature of the Atlantic thermohaline circulation (see the schematical illustration in Fig. 4).

4) Data assimilation conducted within a coupled model allows the coupled dynamics to impact the assimilation results through feedback processes between coupled components.

In this case, the ODA based on an ocean observing network provides constrained SSTs to the atmosphere thereby improving the estimate of the atmospheric states. In return, the improved atmospheric momentum, heat and water fluxes may yield improved estimates of background error covariances used in ODA.

3 Experimental design

3.1 Perfect model study "twin" experiments

The proof-of-concept of coupled model data assimilation using an ensemble filtering algorithm has been given in Zhang et al. (2007). There, the results of a primary assimilation test, a long perfect model ODA experiment based on the 20^{th}-century *in situ* temperature observations only, show that the variability of oceanic heat content is reconstructed very well by using coupled dynamics to extract observational signals within the CDA system. The CDA system is able to sustain dynamical balances and the physical consistency among different state variables and different coupled model components.

Reconstruction of oceanic states using coupled model and real observed data is a complex task, in which model bias is a big challenge that would be along the line for long time. This study serves as the first step of our long term efforts toward the reconstruction of oceanic climate variations utilizing models and data. In order to investigate the roles played by initial conditions, external radiative forcings and oceanic observing network play in detecting oceanic variability by data within a coupled system, this study still employs a perfect model study framework, a particular type of observing system simulation experiments (OSSEs) that are based on a real oceanic observing network (OON). Within those OSSEs the complexity of the climate detection issue is decreased by excluding model bias. What follows describes the OSSEs that are used in this study.

First, same as in Zhang et al. (2007), the dataset (monthly-mean) of the 25-year (1976-2000) oceanic/atmospheric/land/sea-ice state variables produced by the GFDL's B-grid climate model (CM2.0) IPCC standard (also called h_1) historical integration defines completely the features of climate variations during this period, called the "truth," which serve as a target for climate detection. This standard IPCC historical run was initialized by a 300-year spinning up with 1860 fixed-year radiative forcings from the previous integration (Stouffer et al. 2004). Then it was integrated with temporally-varying GHGNA radiative forcings from 1861 to 2000. Second, in order to produce daily hypothetical observation data, the IPCC historical integration is re-run starting from 1 Janury 1976 up to 31 December 2000. Model observation data are based on oceanic temperature and salinity profiles from a certain OON described in item 3 of section 3.2. Then the "truth" is projected onto the chosen OON to form the "observed" data. For example, the 20^{th}-century OON only samples the "truth" oceanic temperature at the locations and depths shown in Fig. 5 while the 21^{st}-century OON samples both oceanic temperature and salinity of the "truth" at the locations and depths shown in Fig. 6. As described in Zhang et al. (2007), the sampling process is basically a tri-linear interpolation, also including superimposition of white noise to simulate random observational errors. The standard deviation of the white noise is 0.5°C for temperature and 0.1 PSU for salinity at the sea surface and exponentially decaying to zero at 2000 m depth.

3.2 3 aspects to be examined

Once the model observation data are ready, without worrying about the influence of model bias, we can examine the impact of the following three factors on the detection of oceanic heat content and salinity variability.

1) **Green House Gas and Natural Aerosol (GHGNA) Radiative Forcings:** For a coupled ocean-atmosphere-land-ice system, the GHGNA radiative effect serves as the utmost external forcing. Previous studies have shown that GHGNA radiative effects are directly responsible for a global scale warming trend (e.g. Manabe 1979; Manabe and Stoufer 1979). Question here is: How important are the historical GHGNA radiative forcings in detecting oceanic variability using models and data? In other words, how

well does an oceanic observing network samples the historical GHGNA radiative effects given a coupled system? In order to answer the questions above, two types of GHGNA radiative forcings – 1860 fixed-year (Q_0) and temporally-varying historical (Q_t) – are applied to the CM2 integrations in the assimilation experiments. Comparing the assimilation results using Q_0 and Q_t holding everything else as the same we can analyze and discuss the impact of GHGNA radiative forcings on detection skills.

2) Coupled (Oceanic) Initial Conditions (ICs): As shown in Fig. 3, unlike atmosphere having strong internal variability from top to bottom, ocean has relatively strong variability in upper and very week variability in deep. Since the availability of oceanic observations is limited within upper oocean (up to 500 m for XBT and up to 2000 m for ARGO, for instance) and assimilation time length is usually limited (from years to decades), we are concerned how oceanic ICs from which the assimilation starts impact the assimilation skill. Two sets of ensemble initial conditions described below, which contain different oceanic states, i.e. the controlled (denoted by IC_c) and the forced (denoted by IC_f), are used to examine the impact of initial conditions on the climate detection.

The IC_c is formed by combining the atmosphere and land states at 00UTC 1 January of years 0041, 0042, 0043, 0044, 0045 and 0046 with the ocean and ice state at 00UTC 1 January 0044 of the GFDL IPCC control run using 1860 fixed-year GHGNA radiative forcings. The IC_f is formed by combining the atmosphere and land states at 00UTC 1 January of years 1973, 1974, 1975, 1976, 1977, 1978 with the ocean and ice state at 00UTC 1 January 1976 of the GFDL IPCC h_3 historical run using temporally-varying GHGNA radiative forcings during the period from 1861 to 2000. The IPCC control/h_3 historical run was initialized by the coupled states at the 300^{th}-year/380^{th}-year spin up with 1860 fixed-year radiative forcings from the previous integration (Stouffer et al. 2004). Since they are driven by different GHGNA radiative forcings for 115 years, the oceanic states in IC_c and IC_f will be shown to be very different. Comparing the assimilation results from IC_c and IC_f with the same other conditions we can investigate the impact of coupled (oceanic) ICs on assimilation quality.

3) Oceanic Observing Network (OON): What scale variability in climate variations can be resolved by an oceanic observing system is a critically-concerned question in climate assessment using models and data. Two oceanic observing networks – the 20^{th}-century OON and the 21^{st}-century OON – are examined in this study.

The network of the 20^{th}-century vertical profiles (also referred to as N_{XBT}) is taken from World Ocean Database (WOD) maintained by National Oceanographic Data Center (NODC). The profile types are largely the same as used by Levitus (2005) for World Ocean Analysis (WOA), primarily from XBT (Expendable Bathythermograph), but also from CTD (Conductivity-Temperature-Depth), DRB (Drifting Buoy), OSD (Ocean Station Data), UOR (Undulating Oceanographic Recorder) and MRB (Moored Buoy). XBTs are the largest single source of oceanic temperature data, being distributed primarily along commercial shipping routes. Their spacial coverage is inhomogeneous, and particularly less accessible in the Arctic and Southern Oceans. Since salinity data are so sparse, only temperature data are considered for the 20^{th}-century OON. Figure 5 shows the locations of the 20^{th}-century OON for January 1986 (left) and 1991 (right) profiles whose depth exceeds 500 m (upper) and 1000 m (lower) [corresponding total profiles shown in Fig. 4 of Zhang et al. (2007)]. Compared to Fig. 4 of Zhang et al. (2007), Fig. 5 shows a dramatic drop in the number of profiles with depth. For example, less than one third of all profiles extend below 500 m; and less than 1 in 30 extend below 1000 m. Some of the XBT profiles can reach a depth of 500 m while profiles below 1000 m are provided mostly by the vertically-high resolution CTD.

In order to focus on the capability of ARGO profiles, here the 21^{st}-century OON includes only the ARGO deploy (also referred to as N_{ARGO}), which excludes altimetry data and conventional shipping-route-based measurements. Particularly, since the ARGO deploy is not finished yet, the 2005 ARGO network as shown in Fig. 6 for January 2005 temperature (left) and salinity (right), is used in this study. (The impact of assimilating altimetry data, a part of the real 21^{st}-century oceanic observing system, will be examined in a separate study.) Figure 6 shows that unlike N_{XBT}, N_{ARGO} has nearly uniform spatial coverage, especially in the Southern Hemisphere where the coverage of N_{ARGO} is much better than the coverage of N_{XBT}. In addition, the number of profiles in N_{ARGO} does not decrease significantly with depth [Compare the profiles below 1000 m (lower panels) to ones below 500 m (upper panels)].

3.3 4 assimilation experiments and 2 model simulations

Once the subsets of hypothetical oceanic observations based on different OONs are ready, the following 4 assimilation experiments are conducted (although a CDA framework is employed, since only oceanic observations are actually assimilated all assimilation experiments in this study are called ODA):

Exp-$\mathbf{IC}_c\mathbf{Q}_0\mathbf{N}_{XBT}$: using the 20^{th}-century OON, 1860 fixed-year GHGNA radiative forcings and controlled initial conditions, IC_c, which do not contain any information about temporally-varying radiative forcings.

Since only temperature with non-uniform spatial distribution is sampled in the 20^{th}-century OON and fixed-year radiative forcings are used in the model integrations, this assimilation experiment is the hardest scenario for detecting climate variability.

Exp-$\mathbf{IC}_c\mathbf{Q}_t\mathbf{N}_{XBT}$: same as Exp-$\mathrm{IC}_c\mathrm{Q}_0\mathrm{N}_{XBT}$ except for using temporally-varying GHGNA radiative forcing in the assimilation model integration.

By comparing the results of this experiment with those of Exp-$\mathrm{IC}_c\mathrm{Q}_0\mathrm{N}_{XBT}$, we try to understand the impact of temporally-varying GHGNA radiative forcings on the climate detection problem.

Exp-$\mathbf{IC}_f\mathbf{Q}_t\mathbf{N}_{XBT}$: same as Exp-$\mathrm{IC}_c\mathrm{Q}_t\mathrm{N}_{XBT}$ except for using forced initial conditions, IC_f, which contain information of temporally-varying GHGNA radiative forcings.

Comparison of results from Exp-$IC_cQ_tN_{XBT}$ and Exp-$IC_cQ_0N_{XBT}$ acknowledges us the sensitivity of detection quality to the initial states from which the assimilation starts.

Exp-$IC_fQ_tN_{ARGO}$: same as Exp-$IC_fQ_tN_{XBT}$ except for using the 21^{st}-century OON, N_{ARGO}, to replace N_{XBT}.

With the replacement of N_{ARGO} that provides both temperature and salinity observations, this experiment is expected to represent the best scenario for detecting climate variability.

As the references for verification, the following two model control integrations (or called free model runs) with no data constraint are also conducted:

Ctl-IC_cQ_0: Initialized from IC_c and using the 1860 fixed-year GHGNA radiative forcings.

Ctl-IC_fQ_t: Initialized from IC_f and using temporally-varying GHGNA radiative forcings.

4 Variability of oceanic heat content

These 4 ODA experiments described in the last section have been conducted within the GFDL CDA system. All ODA experiments in this study use a multi-variate analysis scheme (indicated schematically by the red arrows in Fig. 2), in which each observation (oceanic temperature denoted by T^{obs}, or oceanic salinity denoted by S^{obs}) is allowed to impact all oceanic state variables (i.e. temperature, salinity and currents). The top 50 m oceanic observations in particular are allowed to directly impact the sea-surface wind stress to increase the constraint of oceanic observations to the coupled model in the absence of atmospheric data constraint. As described in Zhang et al. (2007), a weighting function $\Omega(a,d)$ (Gaspari and Cohn 1999) is used for covariance localization to limit the noise in covariance estimate by a finite-ensemble size (Hamill et al. 2001). Given the sparsity of oceanic observations in space and time and ocean model drift (associated with weak internal variability), it is important to apply the filtering technique to the horizontal and the vertical domain and a time window (Zhang et al. 2005). In order to maintain the physical balance mostly, a uniform 1000 km horizontal correlation scale [the parameter a in $\Omega(a,d)$] is used for all analyzed variables (U,V,T,S and τ_x, τ_y) in all experiments (here d is the real distance between observation location and the analyzed grid point). Vertically, the value of a is set to be the thickness of two gridboxes above or below the observational location. Since the observational impact is extended according to the thickness of the gridbox around the bottom of a profile, this setting of a is expected to reduce the vertical discontinuity of the analysis adjustment at the bottom of observed profiles. For example, if the bottom of profile is around 1000 m, the observational impact at the bottom is extended to around 1360 m and if the bottom of profile is around 2000 m, the observational impact at the bottom is extended to around 2850 m by the function $\Omega(a,d)$. Other parameters are the same as in Zhang et al. (2007).

4.1 Impact of temporally-varying GHGNA radiative forcings

The motivation to conduct Exp-IC$_c$Q$_0$N$_{XBT}$ and Exp-IC$_c$Q$_t$N$_{XBT}$ is to try to answer the following two questions: First, given that the atmosphere serves as the driver of oceanic circulations, the different radiative forcings in the atmosphere may make the assimilation model slightly biased. How does the ODA perform with such a slightly biased oceanic model? Second, how much information of temporally-varying GHGNA radiative forcings is represented by an OON?

Time series of oceanic heat content, i.e. potential temperature anomalies averaged over top 700 m (Fig. 7) and 2000 m (Fig. 8), from 4 assimilation experiments are shown for individual ocean basins and the world ocean in Figs. 7 and 8. In those Figs., Exp-IC$_c$Q$_0$N$_{XBT}$ and Exp-IC$_c$Q$_t$N$_{XBT}$ lines are plotted by dashed- and solid-red lines, respectively. As shown by the background colors in Fig. 5, the ocean basins examined here are the same as in Zhang et al. (2007) following Levitus et al. (2000; 2005). The 2 free coupled model runs, Ctl-IC$_c$Q$_0$ and Ctl-IC$_f$Q$_t$, are plotted by dashed- and solid-green lines, respectively as reference. The former (dashed-green line) serves as the control case of Exp-IC$_c$Q$_0$N$_{XBT}$ with no data constraint for recovering the target (or the truth, plotted by black lines – again the GFDL IPCC h_1 historical run). For comparison, all anomalies are computed using the climatology of the "truth." In all basins, the heat content of the "truth" (black lines in Fig. 7) shows a non-uniform warming trend during the 25-year target period, being weakest in the Arctic and strongest in the Indian Ocean, while the control (dashed-green) with the fixed-year forcings only shows the non-trend oscillations. The world oceanic heat content in the "truth" shows a warming trend of 0.2^{o}C during the 25-year period, with two interuptions corresponding to the volcanic activities during the early 1980's and 1990's.

Figures 7 and 8 also show that after a few years of spinup, the heat content decadal variability and multi-decadal trend over top 700 m and top 2000 m are retrieved well by both Exp-IC$_c$Q$_0$N$_{XBT}$ and Exp-IC$_c$Q$_t$N$_{XBT}$ in all basins and the world ocean. The 20-year averaged root mean squared (RMS) and mean errors are dramatically reduced through both ODA experiments comparing to the free model simulation (Ctl-IC$_c$Q$_0$) (Compare columns 4 and 5 to column 1 in Table 1 and 2). In particular, both assimilations reduce heat content RMS errors as the same rate (56% for top 700 m and 42% for top 2000 m) for the world ocean and slightly different rate in individual basins. These results show that the assimilation with fixed-year or temporally-varying GHGNA radiative forcings produce overall equivalent assimilation quality.

Quantitative error statistics presented in columns 4 and 5 of Table 1 and 2 show that the assimilation skill (for both experiments Exp-IC$_c$Q$_0$N$_{XBT}$ and Exp-IC$_c$Q$_t$N$_{XBT}$) is different for each basin. The best is the North Pacific Ocean (the RMS error reduction is around 70% for both top 700 m and top 2000 m) and the worst is the North Indian Ocean (the RMS error reduction is around 15% for top 700 m but the RMS errors are increased for top 2000 m by both assimilations). Next, starting from how and why the assimilation has different performance in different basins, we try to understand the mechanism why the temporally-varying GHGNA radiative forcings have little impact on assimilation quality.

The adjustment of oceanic states produced by ODA in a CDA system is determined by three factors: 1) direct and indirect oceanic data constraints, 2) dynamical constraints due to the interactions of oceanic circulations in different ocean basins and/or the spatial structure of gyres, and 3) external forcing constraints imposed by other components of the coupled model, e.g. Ekman friction effects from the atmospheric wind stress at the sea-surface and freshwater forcings from precipitation and ice melting etc. Item 3) usually refers to as the waters close to the sea-surface; once external forcings drive out oceanic circulations, the effects shall be accounted into the dynamical constraint of item 2). A dynamical constraint refers to as the tendency of a model to maintain an existing circulation structure according to the law of fluid motions. In data assimilation, dynamical constraint is a double edged sword. On one hand, the model dynamics play an essential role in extracting the observational information. This is why assimilation skills always strongly relies on the covariance model being used and in sparse-data or no-data regions the assimilation can still make adjustments from data constraints in neighboring regions. On the other hand, a too strong dynamical constraint means that an efficient data constraint becomes difficult due to the strong inertia of circulations. Usually, data constraint produces relatively faster adjustments than dynamical or external forcing constraints.

Although there is a sparse data coverage in the Southern Ocean and almost none in the Arctic Ocean, the ODA process is still able to gradually nudge the heat content anomalies in both ocean basins towards the truth. This is due to the dynamical constraint of the coupled model responding to the data adjustments in other oceans and it causes the RMS errors of the Southern Arctic Oceans reduced around 40% and 30% respectively, in a two-decade time scale. These dynamical constraints include interactions between the circulations in the Southern Ocean and other neighbouring oceans such as the South Pacific etc., as well as the ice-water interactions and ice-atmosphere flux exchanges in the Arctic. As pointed in Zhang et al. (2007), the spinup time scale in the ODA is strongly associated with the OON's density; the assimilation adjustment in these two oceans is therefore the slowest compared to other basins. Since data constraint is dominant in the upper oceans, except for the Arctic and Southern Oceans, the interannual variability of the truth heat content over top 700 m of other oceans is well reproduced (Fig. 7) in both experiments. Because of the relative sparseness of data coverage in the Indian Ocean in the 20^{th}-century OON, a clear difference between the assimilated heat content anomaly and the truth can be distinguished in the South and North Indian Oceans as well as the entire basin. Due to the reduced data constraint by the depth (see left panels of Fig. 5) the assimilation bias increases in deep ocean (Fig. 8), especially in the regions where data becomes very sparse or non-existent (the North Indian Ocean, for instance). In particular, the rich spectrum of active circulations driven by the Indian monsoon in the North Indian Ocean and the heat and salt exchanges between the Indian and Pacific Oceans by the through flows over the Indoniesian archipelagos make more difficult for the ODA to resolve the sub-annual variability in that region. Due to dynamical constraints like the vertical structure of subtropical and/or subpolar gyres in the Pacific and Atlantic Oceans, the large time scale heat content variations and trend can still be detected by the assimilation process down to a depth of 2000 m over there (Fig. 8).

In ODA, oceanic data constraints attempt to immediately adjust oceanic states toward what data sample. Responding to data constraints, dynamical constraints of ocean model blend and absorb data constraint information by a slower time scale. Eventually the balanced states between data and dynamical constraints form the assimilation equilibria. In this process, if we view the basin waterbody as a whole, the atmosphere provides wind stress and heat/water fluxes to join the dynamical constraints. As shown in Zhang et al. (2007), the ODA-generated SSTs have strong impact on these atmospheric conditions. The following results shall illustrate that in the coupled assimilation framework, the role of the GHGNA radiative forcings to drive the atmospheric circulations is negligible relative to the role of the ODA-generated SSTs.

Comparing the results of Exp-IC$_c$Q$_t$N$_{XBT}$ (solid-red lines in Figs. 7 and 8, column 5 in Tables 1 and 2) to Exp-IC$_c$Q$_0$N$_{XBT}$ (dashed-red in Figs. 7 and. 8, column 4 in Tables 1 and 2), it is observed that based on the same OON and starting from the same initial conditions, the heat content variations produced by Exp-IC$_c$Q$_0$N$_{XBT}$ and Exp-IC$_c$Q$_t$N$_{XBT}$ are nearly indistinguishable in most of basins and the world ocean except for the Arctic Ocean. In the Arctic Ocean, a noticeble difference between Exp-IC$_c$Q$_0$N$_{XBT}$ and Exp-IC$_c$Q$_t$N$_{XBT}$ is observed after the spinup of a few years, but comparing to the difference between either assimilation and the control (dashed-green line) it is very small. These results mean that within a few decade assimilation time scale, the temporally-varying radiative forcings do not have significant impact on the reconstruction of the oceanic heat content variations by the ODA in a coupled system. In other words, the information of ocean heat uptake from Q$_t$ to form heat content's interannual variability and decadal trend is sufficiently retrieved by the ODA based on the OON used. Again, the reason is that the ODA-generated SSTs drive the atmospheric circulations dominantly over the temporally-varying GHGNA radiative forcings, which provide the ocean's upper boundary conditions. The phenomenon of the Arctic Ocean implies that for the regions covered by ice the role of GHGNA radiative effects increases and the SSTs' role decreases, but both slightly.

Looking at the spatial distribution of large time scale heat content variations, panel *a* in Fig. 9/10 exhibits the time tendency of the 10-year mean "true" oceanic heat content of top 700/2000 m during the 1980's and the 1990's. Panels *b*, *c*, *d*, *e*, *f* present the error distributions of the 2-decade time tendency for 1 control simulation (*b* for Ctl-IC$_f$Q$_t$) and 4 assimilation experiments (*c*, *d*, *e* and *f* for Exp-IC$_c$Q$_0$N$_{XBT}$, Exp-IC$_c$Q$_t$N$_{XBT}$, Exp-IC$_f$Q$_t$N$_{XBT}$ and Exp-IC$_f$Q$_t$N$_{ARGO}$ respectively). Panels *a* of Figs. 9 and 10 show that the major time variations over the 2 decades (a warming trend in most basins) occur in the regions of the subtropical and subpolar gyres of the Pacific and Atlantic Oceans in the Northern Hemisphere, and the subpolar region of the Southern Hemisphere where the Antarctic circumpolar circulation is active. Although they use the same temporally-varying GHGNA radiative forcings, Ctl-IC$_f$Q$_t$ and the truth still produce different phases for the gyres and the Antarctic circumpolar circulation and the Ctl-IC$_f$Q$_t$'s warming trend is much weaker than the truth in most basins. This happens because these two integrations use different initial conditions at a century ago (see sections 3.1 and 3.2) and they make the different model climate. Both Exp-IC$_c$Q$_0$N$_{XBT}$ and Exp-IC$_c$Q$_t$N$_{XBT}$ mostly retrieve the 2-decade variations over the Pacific and Atlantic Oceans wherever there exists reasonable data coverage. The largest detection errors are distributed over the Southern Ocean, Indian Ocean and North Atlantic; the former two can basically be attributed to the sparseness of data coverage in the 20^{th}-century OON; the latter one is associated with complex factors like the North Atlantic meridional overturning circulation (MOC) and the ice-water interaction etc. This will be discussed more later.

In comparison with Exp-IC$_c$Q$_0$N$_{XBT}$ (panels c in Figs. 9 and 10), Exp-IC$_c$Q$_t$N$_{XBT}$ (panels d in Figs. 9 and 10) has a similar error distribution for the 2-decade heat content time tendency. The similarity of panels c and d in Figs. 9 and 10 suggests that, again, the radiative forcings play little role in detecting the multi-decadal heat content variability. However, Exp-IC$_c$Q$_t$N$_{XBT}$ has a colder tendency over the Labrador Sea and a warmer tendency over the Greenland Sea than Exp-IC$_c$Q$_0$N$_{XBT}$ does. Use of the 'perfect' radiative forcings causing the extra errors on decadal heat content tendency over Labrador Sea and Greenland Sea implies that the heat transport associated with sea-ice processes is very sensitive to a subtle change in model integration environment like the atmospheric radiative forcings. To understand the mechanism of extra errors produced by temporally-varying radiative forcings requires further studies, especially for the response of sea-ice to radiative effects in the atmosphere. This topic lies beyond the scope of this study and shall be addressed in follow-up studies.

4.2 Impact of oceanic initial conditions

In Figs. 7 and 8, dashed-blue lines represent the oceanic heat content variations produced by Exp-IC$_f$Q$_t$N$_{XBT}$ in individual ocean basins and the world ocean. Note that the only difference between Exp-IC$_c$Q$_t$N$_{XBT}$ (solid-red lines) and Exp-IC$_f$Q$_t$N$_{XBT}$ (dashed-blue lines) is the initial conditions from which the assimilation model is initialized (the former is IC$_c$ and the latter is IC$_f$). The solid-green is the control model simulation (without data constraint) starting from IC$_f$ and using the same (temporally-varying) radiative forcings (Q$_t$) as in Exp-IC$_c$Q$_t$N$_{XBT}$ and Exp-IC$_f$Q$_t$N$_{XBT}$, CTL-IC$_f$Q$_t$. Except for the South Indian Ocean, in all other ocean basins and the world ocean the control model simulation starting from IC$_f$ and using Q_t is much warmer than the control run starting from IC_c and using Q_0 (Ctl-IC_cQ_0, dashed-green). Also for most of basins and the world ocean, the "truth" (black lines) lies between Ctl-IC_cQ_0 and Ctl-IC_fQ_t (solid- and dashed-green lines) and therefore for most of basins the Ctl-IC_cQ_0's mean error is negative while the Ctl-IC_fQ_t's mean error is positive (also see columns 2 and 3 in Tables 1 and 2). The warmer/colder bias in IC_f/IC_c leads to the Exp-$IC_fQ_tN_{XBT}$/Exp-$IC_cQ_tN_{XBT}$ assimilation approaches the truth from either side and eventually produces a warmer/colder assimilation bias (compare dashed-blue lines to solid-red lines in Fig. 7 and 8 and mean errors in columns 5 and 6 in Tables 1 and 2). After the spinup of a few years, with their own small scale features, both assimilations capture the interannual variability and decadal trend of oceanic heat content in basins and the world ocean. Although from the time series in Figs. 7 and 8 it's difficult to distinguish the difference of assimilation skills of Exp-$IC_cQ_tN_{XBT}$ and Exp-$IC_fQ_tN_{XBT}$, the quantitative error stististics (compare column 6 to column 5 in Table 1 and 2) show that the use of IC_f improves dramatically the assimilation quality. The RMS's reduction from Exp-$IC_cQ_tN_{XBT}$ to Exp-$IC_fQ_tN_{XBT}$ is around 15-20% in the Atlantic and Pacific Oceans and around 40% in the Indian Ocean while the world ocean gains about 25% RMS error reduction. The biggest improvement is found in the North Indian Ocean – the RMS's reduction over top 2000 m from Exp-$IC_cQ_tN_{XBT}$ to Exp-$IC_fQ_tN_{XBT}$ exceeds 50%.

The dashed-/solid-green lines in Figs. 7 and 8 show that by a centennial time scale, the fixed-year/temporally-varying GHGNA radiative effects can drive out a cold/warm ocean state. Generally, IC_c and IC_f produce different initial shocks for assimilation so as to impact on assimilation skills. Since the coupled model states have already been forced by historical GHGNA records for a long time, the latter is expected to produce smaller initial shocks in Exp-$IC_fQ_tN_{XBT}$ than the former in Exp-$IC_cQ_tN_{XBT}$. Particulary, given the fact that too few observations are available in deep ocean (only some CTD profiles can go deeper than 2000 m), the difference of deep ocean states in IC_c and IC_f have serious impact on ODA initial shocks. Furthermore, due to the nature of low-frequency of deep ocean circulations (Fig. 3) the assimilation shocks caused by different deep ocean states in IC_c and IC_f shall produce quite different assimilation quality in a few decade period. This generally explains why the assimilation quality has a big jump from Exp-IC$_c$Q$_t$N$_{XBT}$ (columns 5 in Table 1 and 2) to Exp-IC$_f$Q$_t$N$_{XBT}$ (columns 6 in Table 1 and 2) and the improvement for top 2000 m is greater than the improvement for top 700 m.

In addition, in the coupled system with ODA only (no data constraint in atmosphere), besides oceanic initial conditions, depending on different basins the sufficiently-forced atmospheric initial conditions by Q$_t$ also have impact on ODA assimilation skills. In this view, the difference of the performance of Exp-IC$_c$Q$_t$N$_{XBT}$ and Exp-IC$_f$Q$_t$N$_{XBT}$ over the North Indian Ocean is quite interesting. From the analyses and discussions in the previous section, we know that the equilibrium state in ODA is balanced by the three torques exerted by data, dynamical and external forcing constraints. As mentioned before, being confined by continents the North Indian Ocean lacks large scale interior circulations like the subtropical Pacific and Atlantic gyres. Instead, the variability of its circulations is mainly driven by the Indian monsoon system and influenced by the adjacent/marginal seas through heat and salt exchanges. Due to the weak dynamical constraint, the ODA equilibrium in the North Indian Ocean, unlike that of other ocean basins, is mainly determined by the data and external forcing constraints. Due to sparse observation coverage in the Indian Ocean (see Fig. 5 and Fig. 4 in Zhang et al. 2007), the ODA-generated SST constraint for the atmosphere is limited in this region and therefore the atmospheric flows in Exp-IC$_c$Q$_t$N$_{XBT}$ and Exp-IC$_f$Q$_t$N$_{XBT}$ basically sustain their own variability. Comparing the surface forcings in Exp-IC$_c$Q$_t$N$_{XBT}$ and Exp-IC$_f$Q$_t$N$_{XBT}$, it is found that the τ_x, τ_y errors of Exp-IC$_c$Q$_t$N$_{XBT}$ are significantly greater than ones of Exp-IC$_f$Q$_t$N$_{XBT}$. Because of better data coverage in the upper ocean relative to deeper, the difference between Exp-IC$_c$Q$_t$N$_{XBT}$ and Exp-IC$_f$Q$_t$N$_{XBT}$ assimilation skills in top 700 m is smaller than in top 2000 m. Again the combination of larger external forcing errors, sparse oceanic observations and weak dynamical constraints leads to a quite low Exp-IC$_c$Q$_t$N$_{XBT}$ assimilation skill in the North Indian Ocean while once the surface forcings in this region are improved in Exp-IC$_f$Q$_t$N$_{XBT}$ its assimilation skill is greatly improved.

The big difference of the 2-decade time tendency of heat content in Exp-IC$_c$Q$_t$N$_{XBT}$ and Exp-IC$_f$Q$_t$N$_{XBT}$ (comparing panel e to panel d in Figs. 9 and 10) occurs at the Southern Ocean and the North Atlantic, especially in their deep oceans. Basically over the Southern Ocean Exp-IC$_f$Q$_t$N$_{XBT}$ has a weaker warm trend while Exp-IC$_c$Q$_t$N$_{XBT}$ has a stronger warm trend. This can be explained by the warmer/colder initial states from which Exp-IC$_f$Q$_t$N$_{XBT}$/Exp-IC$_c$Q$_t$N$_{XBT}$ starts (see the solid-/dashed-green lines in Fig. 8). In the Southern Ocean, the dynamical constraint in ODA brings the heat content to gradually approach the truth from the either side so Exp-IC$_f$Q$_t$N$_{XBT}$/Exp-IC$_c$Q$_t$N$_{XBT}$ sustains a weaker/stronger warm trend. The difference of time tendency error reduction over the Labrador Sea and Greenland Sea between Exp-IC$_c$Q$_t$N$_{XBT}$ and Exp-IC$_f$Q$_t$N$_{XBT}$ means that at the far North Atlantic, the decadal heat content variations especially in deep ocean are sensitive to the initial conditions too. Again, due to the existence of deep convections at the North Atlantic MOC which is related to the heat and salt transport from ice-water interactions and other complex processes, the mechanism over the North Atlantic Ocean needs more research work for further understanding.

The analyses above tell us that a long time model spinup by temporally-varying GHGNA radiative forcings reduces initial assimilation shocks, especially in deep ocean. The forced ICs by the historical GHGNA records render smaller ODA initial shocks and help increase the effect of data constraints, and the use of the forced ICs therefore produces better assimilation skills. Given that both the 20th- and 21st-century OONs do not provide significant observations below 2000 m, the analyses above also suggests that when we make numerical climate prediction, a long time spinup assimilation for forecast initialization might be necessary.

4.3 Impact of 20th/21st-century OON (N$_{XBT}$/N$_{ARGO}$)

The 21st-century OON, N$_{ARGO}$ (ARGO network), has two substantial differences from the 20th-century OON: 1) Unlike N$_{XBT}$, N$_{ARGO}$ has almost same amount of salinity profiles as temperature's (see the upperleft and the lowerleft of Fig. 6) and 2) ARGO floats are initially deployed on a 3^ox3^o mesh system globally down to 2000 m. The ARGO deploy provides a much more uniformly distributed network both horizontally and vertically than the 20^{th}-century OON.

Replacing N_{XBT} by N_{ARGO} as shown in Fig. 6, Exp-$IC_fQ_tN_{XBT}$ ODA experiment is re-run as Exp-$IC_fQ_tN_{ARGO}$ (solid-blue lines in Fig. 7 and 8, column 7 in Tables 1 and 2). From Exp-$IC_fQ_tN_{XBT}$ (dashed-blue lines in Figs. 7 and 8, column 6 in Tables 1 and 2) to Exp-$IC_fQ_tN_{ARGO}$, the systematic improvement on assimilation skills of oceanic heat content appears in the whole upper 2000 m in which the world ocean's RMS reduction is around 20%. For top 700 m, the improvement is found, from most to least, in the Southern Ocean (error reduction by 36%), the Indian Ocean (23%) and the Arctic Ocean (14%) while for the Atlantic and Pacific Oceans, the assimilation skills drop. These phenomena can be explained by the data coverage of ARGO network, since as pointed out by AchutaRao et al. (2006), the sampling coverage has a large impact on the inferred temperature variability. Relative to N_{XBT}, N_{ARGO} improves mainly the coverage of temperature samples at high latitudes (especially for the Southern Hemisphere) and deep ocean. For the top (say, top 500 m) Pacific and Atlantic Oceans (especially for the North Pacific and the North Atlantic) the N_{XBT} (Fig. 4 of Zhang et al. 2007) is better than the N_{ARGO} (Fig. 6). Substantial improvements on the assimilation quality of oceanic heat content occur mainly over the Indian Ocean, the Southern Ocean and the Arctic Ocean, especially in deep oceans, where the data coverage of the 20^{th}-century OON is the sparsest. Among these oceans, the greatest enhancement of the assimilation skill is in the North Indian Ocean where the RMS error in top 2000 m is reduced by 30% and the mean error is reduced over 90%. Consequently, the world ocean's RMS and mean errors of top 2000 m are reduced by 20% and 60% respectively.

And also, the improvement of the assimilation quality of oceanic heat content from Exp-$IC_fQ_tN_{XBT}$ to Exp-$IC_fQ_tN_{ARGO}$ is partly due to the indirect data constraint from the salinity observations through T-S covariances. In this case the T-S relationship is appied in two ways: oceanic salinity is adjusted using temperature observations and oceanic temperature is adjusted using salinity observations, while in Exp-IC$_f$Q$_t$N$_{XBT}$ only salinity is adjusted by temperature observations through T-S covariances. In this way, since better physical balances between temperature and salinity are maintained, the assimilation more efficiently extract the observational information by model dynamics. When the real 21^{st}-century observing system (say, N$_{XBT}$ + N$_{ARGO}$) is used for real oceanic analysis, the adjustment using the ARGO salinity would enhance the assimilation quality much more than the case in which only more temperature observations is used.

Due to the substantial increase of data in the Southern Ocean and the Indian Ocean in the 21^{st}-century OON, the estimated time tendency for top 700 m and 2000 m heat content have been improved over these basins in Exp-IC$_f$Q$_t$N$_{ARGO}$ from Exp-IC$_f$Q$_t$N$_{XBT}$ (Compare panel f to panel e in Figs. 9 and 10). Particularly, larger positive temperature errors at the entrance of the Labrador Sea in Exp-IC$_f$Q$_t$N$_{XBT}$ has been eliminated in Exp-IC$_f$Q$_t$N$_{ARGO}$. Given the fact that both the 20^{th}-century and 21^{st}-century OONs sample a reasonable number of observed temperature profiles over the northwest Atlantic, the improvement at the entrance of the Labrador Sea should be attributed to the direct assimilation of salinity observations. The improved thermohaline structure must improve the estimate of deep convections associated with the North Atlantic MOC. In addition, probably owing to the ARGO float's drift by the ocean currents, as shown in Fig. 6, the ARGO deploy contains relatively sparse observations (both temperature and salinity) over the eastern part of the North Atlantic subtropical gyre. This also creates errors for the heat content time tendency in Exp-IC$_f$Q$_t$N$_{ARGO}$. The sensitivity of the estimated heat content time tendency to the density of observations over the eastern North Atlantic region is related to the strong temperature gradient across the North Atlantic subtropical gyre (e.g. see panel b of Fig. 9).

The assmilation skills on oceanic heat content analyzed in this section are consistent with the diagnoses on heat uptake. About the impact of ODA on oceanic heat uptake in the coupled model framework will be discussed in details in a separate study.

5 Variability of oceanic salinity

Given that the 20^{th}-century OON provides temperature observations only, this section seeks answers for the questions: Based on the 20^{th}-century temperature OON, how much can a coupled ensemble filter rebuild the salinity variations by utilizing T-S covariances? With the 21^{st}-century temperature and salinity observing network (ARGO), how well can the coupled ensemble filter reconstruct the interannual variability and decadal trend of oceanic salinity? Comparing to the case assimilating salinity observations, what do we miss if only T-S covariances are used?

5.1 T-S relationship only

Time series of salinity anomalies from 2 control model runs (Ctl-$\mathrm{IC}_c\mathrm{Q}_0$ and Ctl-$\mathrm{IC}_f\mathrm{Q}_t$, dashed-/solid-green lines) and 4 assimilation experiments (Exp-$\mathrm{IC}_c\mathrm{Q}_0\mathrm{N}_{XBT}$, Exp-$\mathrm{IC}_c\mathrm{Q}_f\mathrm{N}_{XBT}$, Exp-$\mathrm{IC}_f\mathrm{Q}_t\mathrm{N}_{XBT}$ and Exp-$\mathrm{IC}_f\mathrm{Q}_t\mathrm{N}_{ARGO}$, i.e. dashed-red, solid-red, dashed-blue and solid-blue lines) for top 700 m and top 2000 m over individual ocean basins and the world ocean are presented in Figs. 11 and 12. As in Figs. 7 and 8, time series of the "true" salinity anomalies are plotted as black lines here too. From Figs. 11 and 12, we find that the integration environment of the assimilation model such as external (GHGNA radiative) forcings, and especially the initial conditions, have much more impact on the salinity assimilation than the temperature assimilation (comparing the difference between solid- and dashed-red lines in Figs. 11 and 12 to the corresponding difference in Figs. 7 and 8). This phenomenon is also reflected in the difference of mean errors between Exp-$\mathrm{IC}_c\mathrm{Q}_0\mathrm{N}_{XBT}$ and Exp-$\mathrm{IC}_c\mathrm{Q}_f\mathrm{N}_{XBT}$ (compare the difference of mean errors in columns 4, 5 in Tables 3 and 4 to corresponding difference in Tables 1 and 2). From Figs. 7 and 8, it is observed that, for most of basins, the assimilations of Exp-$\mathrm{IC}_c\mathrm{Q}_0\mathrm{N}_{XBT}$ and Exp-$\mathrm{IC}_c\mathrm{Q}_f\mathrm{N}_{XBT}$ (using T-S covariances and starting from IC_c) only make significant convergence of salinity anomalies of upper ocean.

RMS error statistics (columns 4 and 5 in Tables 3 and 4) show that except for the Indian Ocean, both assimilations reduce the salinity RMS errors from the free model run. The amptitude of the error reduction of top 700 m (46% for the Pacific and 23% for the world ocean, for instance) is much more than top 2000 m (17% the Pacific and negative for the world ocean). There is almost no difference of RMS error statistics of the assimilation salinity between Exp-IC$_c$Q$_0$N$_{XBT}$ and Exp-IC$_c$Q$_f$N$_{XBT}$ except for the Arctic Ocean where the former is larger than the latter (compare column 5 to column 4 in Table 3 and 4). Combining with RMS error statistics the difference of mean errors between these two assimilations does not mean a meaningful improvement on salinity assimilation skill.

In this coupled system, the salinity adjustment in Exp-IC$_c$Q$_0$N$_{XBT}$ and Exp-IC$_c$Q$_f$N$_{XBT}$ comes from two parts. One is the direct projection from oceanic temperature observations by T-S covariances, and the other is the response of the coupling mechanism to the ODA-generated SSTs. For example, when the atmosphere is driven by the ODA-generated SSTs, as a return, the precipitation and the surface wind stress provided by the atmosphere alter the salinity distribution in the top layer of ocean. Eventually, the adjustment of the top ocean salinity is a combination of the above two factors while the changes of the salinity in deep ocean mainly rely on the response of oceanic circulations to the adjustment of the upper ocean. Since the Ctl-IC$_c$Q$_0$ stays colder and saltier than the "truth," assimilations of Exp-IC$_c$Q$_0$N$_{XBT}$ and Exp-IC$_c$Q$_t$N$_{XBT}$ tend to make the water fresher and warmer in most of basins and the world ocean. Generally, in the tropics the T-S relationship is able to retrieve the variations of top ocean salinity anomalies to some degree due to the linkage between convective precipitation (associated with warm SSTs) and fresher water near surface and a good T-S relationship associated with the isopycnal nature of thermocline oscillations (Zhang et al. 2007). A tropical Pacific example (5^{o}S-5^{o}N, top 200 m) is shown in Fig. 13 where the salinity anomalies in all 4 assimilations follow the "true" variability, in which the salinity anomaly of Exp-IC$_f$Q$_t$N$_{XBT}$ exhibits the smallest error.

In the extratropics and deep oceans, the main role of the T-S covariance-based salinity assimilation from temperature observations is to sustain the dynamical balance. The use of T-S covariances is not sufficient to constrain the salinity anomaly to follow the truth. For example, the salinity assimilation in Exp-IC$_c$Q$_0$N$_{XBT}$ and Exp-IC$_c$Q$_f$N$_{XBT}$ produces a negative salinity time tendency (oceans continue to freshen) in top 2000 m of most basins and the world ocean (panels *c* and *d* in Fig. 14).

A noticeable phenomenon in Exp-IC$_c$Q$_0$N$_{XBT}$ and Exp-IC$_c$Q$_t$N$_{XBT}$ is that negative anomalies of the world ocean salinity overshoot the truth, especially for top 2000 m (see the WORLD OCEAN panel of Fig. 12). i.e., the ocean in these assimilations is too fresh. The Southern Ocean is the main contributor to this overshooting. Here we can use the lines of temperature and salinity anomalies in Ctl-IC$_c$Q$_0$ and Ctl-IC$_f$Q$_t$ (dashed- and solid-green lines in Figs. 7, 8, 11 and 12) to estimate how the assimilation model responds to upper ocean temperature observations to form the top 2000 m salinity anomalies. In top 700 m of the Southern Ocean, the Ctl-IC$_c$Q$_0$ water is colder and fresher than the Ctl-IC$_f$Q$_t$ water (see dashed-/solid-green lines in Figs. 7 and 11), while in top 2000 m, the Ctl-IC$_c$Q$_0$ water is colder and saltier than the Ctl-IC$_f$Q$_t$ water (see dashed-/solid-green lines in Figs. 8 and 12). This implies a negative correlation of the top 2000 m salinity and the upper ocean temperature observations. It is saying that the assimilation model responds to the warming of the top ocean of the Southern Ocean by making the water fresher. During the last 10 years of the assimilation, the averaged T-S covariance in Exp-IC$_c$Q$_0$N$_{XBT}$ (estimated by the Southern Ocean domain-averaged temperature and salinity of top 2000 m) is -5$\times$10^{-5} PSU ^{o}C. Given a warming of 0.25^{o}C and a temperature standard deviation of 0.087^{o}C, regression produces a freshening of -1.5$\times$10^{-4} PSU, The freshening rate is seriously underestimated by the domain-averaging effect, but it does indicate a freshening trend. Understanding the mechanism of the Southern Ocean's freshening trend induced by a warming trend of upper ocean requires further research work on the Southern Ocean's circulations (the Antarctic circumpolar circulation, for instance).

Consistent with the analyses for oceanic heat content in section 4.1, the analyses above for oceanic salinity assimialtion quality further show that the temporally-varying GHGNA radiative forcings do not have much impact on assimilation quality. Understanding why the use of Q$_t$ makes the assimilation of the Arctic Ocean worse requires further research work too.

5.2 Using IC_f

The salinity assimilation errors of Exp-$\mathrm{IC}_f\mathrm{Q}_t\mathrm{N}_{XBT}$ (columns 6 in Tables 3 and 4) are much smaller than the errors of Exp-$\mathrm{IC}_c\mathrm{Q}_0\mathrm{N}_{XBT}$ and Exp-$\mathrm{IC}_c\mathrm{Q}_t\mathrm{N}_{XBT}$ (also see dashed-blue lines in Figs. 11 and 12). The biggest improvement is in the Indian Ocean where the error reduction from Exp-$\mathrm{IC}_c\mathrm{Q}_t\mathrm{N}_{XBT}$ to Exp-$\mathrm{IC}_f\mathrm{Q}_t\mathrm{N}_{XBT}$ is around 40% for top 700 m and 50% for top 2000 m. The deep ocean improvement is greater than the upper (for the world ocean, 30% error reduction in top 700 m and 43% in top 2000 m, for instance). And also, compared to the heat content assimilation improvement (columns 6 in Tables 1 and 2, 23%/27% error reduction for the world ocean top 700 m/top 2000 m, for instance), the salinity assimilation improvement by using IC_f is more dramatically (columns 6 in Tables 3 and 4, 30%/43% error reduction for the world ocean's top 700 m/top 2000 m). In addition, comparing the errors of the 2-decade salinity time tendency in Exp-$\mathrm{IC}_c\mathrm{Q}_0\mathrm{N}_{XBT}$ and Exp-$\mathrm{IC}_c\mathrm{Q}_t\mathrm{N}_{XBT}$ (panels *c* and *d* in Fig. 14) to the salinity tendency errors of Exp-$\mathrm{IC}_f\mathrm{Q}_t\mathrm{N}_{XBT}$ (panel *e*) it is found that the latter reduces the salinity time tendency errors from the corresponding free model run (Ctl-$\mathrm{IC}_f\mathrm{Q}_t$, panel *b*) more greatly than the former two do from Ctl-$\mathrm{IC}_c\mathrm{Q}_0$ (not shown here). We also can see that the salinity time tendency errors of Exp-$\mathrm{IC}_f\mathrm{Q}_t\mathrm{N}_{XBT}$ are much less than ones of Exp-$\mathrm{IC}_c\mathrm{Q}_0\mathrm{N}_{XBT}$ and Exp-$\mathrm{IC}_c\mathrm{Q}_t\mathrm{N}_{XBT}$.

The analyses of heat content assimilation in section 4 have shown that due to the low-frequency nature of oceanic circulations the initial shocks have serious impact on oceanic assimilation skill. Since the T-S relationship derived from model is a weak constraint for salinity, when only T-S covariances are used to transform temperature observational increments to salinity adjustments, the salinity assimilation quality relies on the initial conditions more strongly than the temperature assisilation does. Thus, in this circumstance, the use of favorite initial conditions, e.g., that have the knowledge of long time temporally-varying radiative forcings, is very important to restrict the salinity assimilation errors to a relatively small range.

5.3 Assimilating salinity observations

When the direct salinity observations in the 21^{st}-century OON are used, the salinity assimilation errors in Exp-IC$_f$Q$_t$N$_{ARGO}$ (solid-blue lines in Figs. 11 and 12, columns 7 in Tables 3 and 4) are much smaller than in other cases. (Larger RMS errors of the North Atlantic Ocean salinity in Exp-IC$_f$Q$_t$N$_{ARGO}$ than other cases may be associated with the detailed structure of meridional overturning circulations which will be discussed more in next section.) For most of basins and the world ocean, the salinity anomalies of top 700 m in Exp-IC$_f$Q$_t$N$_{ARGO}$ capture the "true" variations very well after the spinup of a few years. Although the deep ocean spinup takes much longer, the assimilation tends to reconstruct the "true" salinity variability up to a depth of 2000 m eventually. However, a noticeable departure between the salinity anomaly of Exp-IC$_f$Q$_t$N$_{ARGO}$ and the truth still can be found in the South/North Indian and Arctic Oceans. Also it is noticed that after 20 years the Arctic Ocean's ODA salinity anomaly begins to follow the "truth". This slow convergence in the Arctic Ocean may be explained by the response of the Arctic Ocean to the assimilation constraints imposed in the neighboring oceans by direct salinity observations as well as to the forcings from other coupled model components such as the atmosphere, sea-ice and land. Relatively large salinity assimilation errors in the North Indian Ocean, again, can be related to its sensitive response to variations of the Indian monsoon and to the influence of the salt budget of the through flows which connect the Indian Ocean to the Pacific Ocean, and local river runoff.

Oceanic assimilation results constrained by both oceanic temperature and salinity observations can be viewed as equilibrium oceanic states in which oceanic data constraints are balanced by external forcings such as the atmospheric wind stress, heat/water fluxes. By improving surface forcings of ocean, a new coupled data assimilation experiment including both atmospheric and oceanic data assimilation components has improved the estimate of oceanic states. This is especially true for such oceans as the Indian and North Atlantic where oceanic circulations have a more sensitive response to the atmospheric forcings. A complete examination of the impact of atmospheric data constraint on the estimation of oceanic states will be presented in separate studies.

6 The thermohaline structure of the North Atlantic Ocean

The North Atlantic (NA) meridional overturning circulation (MOC) has been recognized as one of the most important oceanic circulations that have important impact on the global climate. The detection of the NA thermohaline structure by an oceanic observing system could serve as the first step for the NA MOC estimation using observed data (including oceanic and atmospheric measurements) and models. Also initialization using the estimated oceanic state might be beneficial for the NA MOC's prediction. This section examines the ability of the ODA component in the GFDL's CDA system to detect the NA thermohaline structure, by analysing the quality of the assimilated oceanic temperature and salinity from 4 ODA experiments. We focus on the upper (200-1000m) and lower (1000-5000m) portions of the North (20^o-70^oN) Atlantic Ocean, which corresponds to the polarward and equatorward heat and salt transport of the NA MOC.

First let us check the convergence of the assimilated oceanic temperature and salinity obtained from these ODA experiments within the NA MOC domain. Figure 15 presents the time series of RMS errors of the assimilated temperature and salinity in the upper 2000 m NA MOC domain for Exp-IC$_c$Q$_0$N$_{XBT}$ (dashed-red), Exp-IC$_c$Q$_t$N$_{XBT}$ (solid-red), Exp-IC$_f$Q$_t$N$_{XBT}$ (dashed-blue) and Exp-IC$_f$Q$_t$N$_{ARGO}$ (solid-blue). The two control model runs (Ctl-IC$_c$Q$_0$/Ctl-IC$_f$Q$_t$) are also plotted in the dashed-/solid-green lines as the reference. Figure 15 shows that compared to the controls, the assimilation errors of both temperature and salinity in all 4 experiments are substantially reduced during the first 15 years (Compare the dahed- and solid-red lines to the dashed green line, and the dashed- and solid-blue lines to the solid-green line). In contrast, only Exp-IC$_f$Q$_t$N$_{ARGO}$ shows a stable convergence during the last 10 years. Further diagnoses reveal that the deep convection associated with the NA MOC encounters a regime shift from an inactive phase to an active phase during the last

10 years. (The estimation and initialization of the NA MOC will be completely analyzed and discussed in a separate follow-up study). On the positive side, due to the existence of the subpolar gyre, the T-S relationship could play an important role in salinity adjustments, which could help somewhat to reconstruct the NA MOC structure. This conveys some hope for estimating the NA MOC using the 20^{th}-century OON, as evidenced by the time series of the assimilated NA temperature and salinity in the upper portion (200-1000m) (panels a and b in Fig. 16). Panels a and b of Fig. 16 show that based on the 20^{th}-century OON, to some degree, the assimilation is able to rebuild the polarward branch of the NA MOC. However, all 3 assimilation experiments using the 20^{th}-century OON show a sharp increase of both temperature and salinity assimilation errors during the last 10 years (Fig. 15). Corresponding jumps are found in the NA temperature and salinity time series in the lower portion (1000-5000m) of the NA MOC (panels c and d in Fig. 16). This means that the 20^{th}-century OON fails to provide sufficient data to resolve the transition from an inactive deep convective regime to an active deep convective regime. It is saying that there is a negative side for the assimilation quality of the North Atlantic Ocean due to the existence of the NA MOC since both its structure and mechanism are so complicated that only using T-S relationship is insufficient to resolve its variability. From Fig. 16, it is observed that even in the Exp-$\mathrm{IC}_f\mathrm{Q}_t\mathrm{N}_{ARGO}$ case (solid-blue line), although sharing a multi-decadal trend with the truth, the deep ocean salinity remains a departure from the truth.

Reconstructing the NA overturning structure with high accuracy is essential for estimating the variation of the NA MOC. This is a complex and challenging task since it is associated with multiple factors such as large-scale heat and salt transport by thermohaline circulations, sea-surface forcings from atmosphere, fresh water forcing from ice and runoff as well as their interaction with the local topographic features. Given the strong linkage between the atmospheric North Atlantic oscillation (NAO) and the NA MOC (Delworth and Greatbatch 2000; Delworth and Dixon 2000), the ODA process in the experiments of the present study are in conflict with the sea-surface forcings from the unconstrained atmosphere. The preliminary results from CDA experiments (belongs to the next phase of this project), which adds an atmospheric data constraint in, show a considerable improvement on the estimate of the NA MOC structure.

7 Conclusions and discussions

This study is the second part of a global oceanic climate study project utilizing the GFDL coupled ensemble data assimilation (CDA) system (Zhang et al. 2007), with a aim at addressing the detection of oceanic variability. As an implementation of stochastic estimation theory, the CDA system solves for a temporally-varying joint probability density function (joint-PDF) of climate state variables by combining the observational PDF and a prior PDF derived from the dynamically-coupled model. The solved joint-PDF, which is represented discretely by a set of ensemble members, is a complete solution of the coupled data assimilation problem. The ensemble mean is the state estimate and higher-order moments measure the uncertainty of the estimate. In this process, observational information – samples of the "truth" – are projected onto the coupling dynamics to form the estimate of climate states. The accuracy of the estimates is influenced not only by the assimilation methodology, but also by the assimilation model's bias as well as the representativeness of observing network.

Based on the methodology described above, this study has examined the detectability of long time scale variability of oceanic heat content and salinity by the 20^{th}-century (temperature only) and the improved 21^{st}-century (both temperature and salinity) oceanic observing system. For this purpose, a perfect model assimilation framework, or called perfect "twin" assimilation experiment, was designed. This is a special type of observing system simulation experiments (OSSEs) based on a real oceanic observing network. In these OSSEs a model simulation with the historical greenhouse gas and natural aerosol (GHGNA) radiative forcings is set as the target (or called the "truth") of assimilation. The model simulation is also used to produce the "observed" data an oceanic observing network to be examined. Given this perfect model study methodology, the influence of model bias is excluded from this study. The "true" oceanic temperature on which a white noise is added is sampled by the 20^{th}-century ocean observing network to form 20^{th}-century ocean "observations"; and the same method is applied to both temperature and salinity to form the 21^{st}-century ocean observations based on the ARGO network. Within the CDA framework, these oceanic model observations are assimilated into the coupled climate model for targeting a 25-year climate variation corresponding to the 1976-2000 historical GHGNA records. These ODA experiments start from different initial conditions (ICs) and use different (i.e. fixed-year or temporally-varying) GHGNA radiative forcings. Two sets of ICs, i.e. the controlled/forced, corresponding to the coupled model states after a long time model spinup by fixed-year/temporally-varying GHGNA radiative forcings, are used in this study.

A series of oceanic data assimilation (ODA) experiments within the coupled model framework is designed to examine the impact of fixed-year/temporally-varying radiative forcings, the controlled/forced ICs and the 20^{th}-/21^{st}-century oceanic observing network upon detection of climate variability. Results established the following findings:

1. Within the 25-year assimilation period, the adjustment of oceanic states is dominated by the data constraint imposed by the assimilated observations while explicit knowledge of temporally-varying GHGNA radiative forcings added to model integration does not produce a significant impact on the assimilation skill. This should not be surprising since the "observations" already implicitly contain the information of temporally-varying radiative forcings.

2. The initial conditions extracted from the GFDL IPCC historical simulation with temporally-varying GHGNA radiative forcings reduce initial assimilation shocks, especially in deep oceans. The small initial assimilation shocks from the forced ICs help increase the effects of data constraint and the forced ICs produce therefore a better assimilation skill than the controlled ICs. Given that both the 20^{th}- and 21^{st}-century in situ measurements do not provide observations below 2000 m (except for some deeper high resolution CTD profiles), when numerical climate predictions are made, a long time assimilation spinup for initialization may be necessary.

3. Comparing the assimilation using the 20^{th}-century XBT observing network to the

assimilation using the 21^{st}-century ARGO observing network, we found that both oceanic observing networks provide adequate samples to capture the decadal/multi-decadal trend and interannual variability of heat content. However, due to the isopycnal nature of oceanic circulations and fresh water forcings at high latitudes, the salinity observations provided by the ARGO network give significant information for reconstructing the thermohaline structure of oceanic states with a high accuracy, and they are therefore very important for global oceanic climate studies. In particular, the salinity observations play a critically-important role for correctly estimating deep convections at the North Atlantic meridional overturning circulation.

4. In tropical oceans, the coupling mechanism produces a strong T-S correlation (e.g. the convective precipitation induced by a warmer SST freshens the surface-near ocean). Therefore the use of T-S covariances in the filter is able to capture the basic features of salinity variability based on in situ temperature measurements only. This conveys a hope that, when we use the real data (temperature only) to estimate the 20^{th}-century climate states, the use of T-S covariances may retrieve some basic features of salinity variability.

As the first step of efforts for estimation of the multi-decadal variability of historical climate variations and its forecast initialization, this study uses the perfect model (identical twin experiment) framework; although this study successfully demonstrated the creditability of the CDA system to detect both the decadal/multi-decadal trend and the interannual variability of oceanic heat content and salinity, we recognized the obtained results may be overly optimistic. The ODA-generated variability resulting from data constraints contains both what data sample and an artifact of data sparseness (see the NORTH INDIAN OCEAN panel in Fig. 8, for instance). The latter may become severe in the presence of model bias. As we apply the ODA approach to the real observations, the model bias issue can be a big challenge. It is difficult to even identify what part of the ODA-generated variability is an artifact of sampling.

In follow-up studies, on one hand, an imperfect "twin" experiment including two coupled GCMs that are biased each other are designed to well define the ODA's "bias" issue brought by model bias, and the imperfect twin assimilation framework also is used to seek the solution of the problem. On the other hand, we realized that, under the coupled model system framework, the oceanic states at the ODA's equilibrium represent the balance of three torques exerted by data constraint, dynamical constraint and external forcing constraint. In this study, external forcings from other components of the coupled model (e.g. the wind stress from atmosphere, which is a leading-order term of external forcings) remain as free modes responding to the ODA-generated sea-surface conditions. This can restrict the efficacy of the ODA's data constraint. Results of CDA experiments which include both oceanic and atmospheric data constraints will be reported by follow-up studies, but they do show that the estimate of oceanic states in individual ocean basins and the world ocean is improved considerably due to the improved ocean external forcings. The correction of external forcings produced by the atmospheric data constraint in a fully-coupled assimilation framework is expected to relax the oceanic model bias and therefore improve the estimate of historical oceanic states using real observed data. Initial estimates of coupled oceanic/atmospheric/sea-ice/land states from 1980-2006 have been done using 24 ensemble members to assimilate real observed oceanic data and the atmospheric NCEP/NCAR reanalysis data. Preliminary results from a set of retrospective one year ENSO (El Nino-Southern Oscillation) forecasts show a significantly improved skill over our 3D-Var assimilation system. Refined versions of the CDA system which for example take model bias correction into account are expected to further improve the estimates of the coupled states and enhance the accuracy of numerical climate predictions. In order to widen the prior PDF and reduce model biases, a multi-model ensemble assimilation system which brings the GFDL's B-grid (CM2.0) and finite-volume (CM2.1) coupled models together to produce error statistics for filtering process is under tests.

In addition, this study uses in situ oceanic measurments only. As an important part of the 21^{st}-century oceanic observing system, the satellite altimeter data contain integrated information of the vertical thermohaline structure and the use of altimeter data is also expected to help relax the model bias problem. How to use altimeter data to build the vertical structure of oceanic circulations shall be an important aspect that will be explored in next efforts.

ACKNOWEDGEMENT

The authors would like to thank Drs. C. T. Gordon and Qian (Scott) Song, for their comments on earlier versions of this manuscript. Thanks go to Dr. Guijun Han for her suggestions in processing observation data during her visit at GFDL. Thanks also go to F. Zeng, Mike Spelman, Z. Liang and H. Lee for their help on model configuration issue. The authors wish to express their special appreciation to F. Zeng who frequently provided suggestions on data processing and visualization. The authors thank two anonymous reviewers for their thorough examination and comments that are very useful for improving the manuscript.

REFERENCES

AchutaRao, K. M., B. D. Santer, P. J. Gleckler, K. E. Taylor, D. W. Pierce, T. P. Barnett and T. M. L. Wigley, 2006: Variability of ocean heat uptake: Reconciling observations and models. *J. Geophys. Res.* **111**, C05019, doi:10.1029/2005JC003136.

Cabanes, C., A. Cazenave and C. Le Provost, 2001: Sea level rise during past 40 years determined from satellite and in situ observations, *Science*, **294**, 840–842.

Carton, J. A., B. S. Giese and S. A. Grodsky, 2005: Sea level rise and the warming of the oceans in the simple ocean data assimilation (SODA) ocean reanalysis. *J. Geophys. Res.* **110**, C09006, doi:10.1029/2004JC002817.

Delworth, T. L. and R. J. Greatbatch, 2000: Multidecadal theermohaline circulation variability driven by atmospheric surface flux forcing. *J. Climate*, **13**, 1481–1495.

Delworth, T. L. and K. Dixon, 2000: Implications of the recent trend in the Arctic/North Atlantic oscillation for the North Atlantic thermohaline circulation. *J. Climate*, **13**, 3721–3727.

Delworth, T. L., A. Rosati, Ronald J. Stouffer, Keith W. Dixon, John Dunne, Kirsten L. Findell, Paul Ginoux, Anand Gnanadesikan, C. T. Gordon, Stephen M. Griffies, Rich Gudgel, Matthew J. Harrison, Isaac M. Held, Richard S. Hemler, Larry W. Horowitz, Stephen A. Klein, Thomas R. Knutson, Shian-Jiann Lin, V. Ramaswamy, M. Daniel Schwarzkopf, Joseph J. Sirutis, Michael J. Spelman, William F. Stern, Michael Winton, Andrew T. Wittenberg, Bruce Wyman, A. J. Broccoli, R. J. S. V. Balaji, Joellen Russell, Rong Zhang, John A. Beesley, Jian Lu, William F. Cooke, Jeffrey W. Durachta, Amy R. Langenhorst, Hyun-Chul Lee, Fanrong Zeng, K. A. Dunne, P. C. D. Milly, Paul J. Kushner, Sergey L. Malyshev and Elena Shevliakova, 2006: GFDL CM2 global coupled climate models, Part I: Fornulation and simulation characteristics. *J. Climate*, **19(5)**, 643–674.

Fedorov, A. V. and S. G. Philander, 2001: Is El Niño changing? *Science*, **288**, 1997–2001.

Francis, R. C. and S.R. Hare., 1994: Decadal-scale regime shifts in the large marine ecosystems of the Northeast Pacific: a case for historical science. *Fish. Oceanogr.*, **3**, 279–291.

Gent, P. R., and G. Danabasoglu, 2004: Heat uptake and the thermohaline circulation in the Community Climate System Model, version 2. *J. Climate.*, **17(10)**, 4058–4069.

Gnanadesikan, A., Keith W. Dixon, Stephen M. Griffies, Thomas L. Delworth, Matthew J. Harrison, Isaac M. Held, William J. Hurlin, Ronald C. Pacanowski, Anthony Rosati, Bonita L. Samuels, Michael J. Spelman, Ronald J. Stouffer, Michael Winton, Andrew T. Wittenberg, John P. Dunne, V. Balaji, Marcelo Barreiro, Joellen Russell, Qian Song, Colm O. Sweeney, Rong Zhang, J. Anthony Beesley, Gabriel Vecchi, William F. Cooke, Hyun-Chul Lee, Zhi Liang, Giang Nong, Fanrong Zeng, Rudiger Gerdes, 2006: GFDL CM2 global coupled climate models, Part II: The baseline ocean simulation. *J. Climate.*, **19(5)**, 675–697.

Gent, P., G. Danabasoglu, 2004: Heat uptake and the thermohaline circulation in the community climate system model, version 2. *J. Climate*, **15**, 4058–4069.

Griffies, S. M., M. J. Harrison, R. C. Pacanowski and A. Rosati, 2003: A Technical Guide to MOM4. *GFDL Ocean Group Technical Report*, No. 5, Princeton, NJ 08542, NOAA/Geophysical Fluid Dynamics Laboratory, 295 pp.

Griffies, S. M. and R. W. Hallberg, 2000: Biharmonic friction with a Smagorinsky-like viscosity for use in large-scale eddy-permitting ocean models. *Mon. Wea. Rev.,* **128**, 2935–2946.

Hunke, E. C., and J. K. Dukowicz, 1997: An elastic-viscous-plastic model for sea ice dynamics, *J. Phys. Oceanogr.*, **27**, 1849–1867.

Manabe, S., 1979: Effect of increasing the CO2 concentration on the climate of a general circulation model. *In Carbon Dioxide Effects Research and Assessment Program: Workshop on the Global Effects of Carbon Dioxide from Fossil Fuels*, U.S. Dept. of Energy, Office of Health & Environmental Research, Washington, DC, Springfield, VA: NTIS, 100–101.

Manabe, S., and R. J. Stouffer, 1979: A CO2-climate sensitivity study with a mathematical model of the global climate. *Nature*, **282(5738)**, 491–493.

Mantua, N.J., S.R. Hare, Y. Zhang, J.M. Wallace, and R.C. Francis, 1997: A Pacific interdecadal climate oscillation with impacts on salmon production. *Bulletin of the American Meteorological Society*, **78**, 1069-1079.

Rahmstorf S., 1995: Bifurcations of the Atlantic thermohaline circulation in response to changes in the hydrological cycle. *Nature*, **378**, 145–149.

Saji, N. H., B. N. Goswami, P. N. Vinayachandran and T. Yamagata, 1999: A dipole mode in the tropical Indian ocean, *Nature*, **401**, 360–363.

Stouffer, R. J., A. J. Weaver and M. Eby, 2004: A method for obtaining pretwentieth century initial conditions for use in climate change studies. *Clim. Dyn.*, **23**, 327–339.

Winton, M., 2000: A reformulated three-layer sea ice model. *J. Atmos. Ocean. Tech.*, **17**, 525–531.

Wittenberg, A. T., 2002: ENSO response to altered climates. Ph.D. thesis, Princeton University, 475pp.

Wittenberg, A. T., 2004: Extended wind stress analyses for ENSO. *J. Climate*, **15**, 2526–2540.

Zhang, Y., J.M. Wallace and D.S. Battisti, 1997: ENSO-like interdecadal variability: 1900-93. *J. Climate*, **10**, 1004-1020.

Zhang, S. and J. L. Anderson, 2003: Impact of spatially and temporally varying estimates of error covariance on assimilation in a simple atmospheric model. *Tellus,* **55A**, 126–147.

Zhang, S., M. J. Harrison, A. T. Wittenberg, and A. Rosati, 2005: Initialization of an ENSO forecast system using a parallelized ensemble filter. *Mon. Wea. Rev.,* **133**, 3176–3201.

Zhang, S., M. J. Harrison, A. Rosati and A. T. Wittenberg, 2007: System design and evaluation of coupled ensemble data assimilation for global oceanic climate studies. *Mon.*

Wea. Rev., **135**, 3541–3564.

TABLE CAPTIONS

Table. 1 The time mean RMS of oceanic temperature errors (^{o}C) over top 700 m during the last 20 years in 2 control and 4 assimilation experiments/the RMS's reduction (%) of assimilation from the case it is compared to (for Exp-IC$_c$Q$_0$N$_{XBT}$ the RMS's reduction is from Ctl-IC$_c$Q$_0$; for Exp-IC$_c$Q$_t$N$_{XBT}$ the reduction is from Exp-IC$_c$Q$_0$N$_{XBT}$; for Exp-IC$_f$Q$_t$N$_{XBT}$ the reduction is from Exp-IC$_c$Q$_t$N$_{XBT}$; for Exp-IC$_f$Q$_t$N$_{ARGO}$ the reduction is from Exp-IC$_f$Q$_t$N$_{XBT}$), the mean errors (10^{-2} ^{o}C) of 4 assimilation and 2 model simulation experiments are listed in parentheses

Table. 2 Same as Table 1 but for top 2000 m

Table. 3 The time mean RMS of oceanic salinity errors (PSU) over top 700 m during the last 20 years in 2 control and 4 assimilation experiments/the RMS's reduction (%) of assimilation from the case it is compared to (for Exp-IC$_c$Q$_0$N$_{XBT}$ the RMS's reduction is from Ctl-IC$_c$Q$_0$; for Exp-IC$_c$Q$_t$N$_{XBT}$ the reduction is from Exp-IC$_c$Q$_0$N$_{XBT}$; for Exp-IC$_f$Q$_t$N$_{XBT}$ the reduction is from Exp-IC$_c$Q$_t$N$_{XBT}$; for Exp-IC$_f$Q$_t$N$_{ARGO}$ the reduction is from Exp-IC$_f$Q$_t$N$_{XBT}$), the mean errors (10^{-2} PSU) of 4 assimilation and 2 model simulation experiments are listed in parentheses

Table. 4 Same as Table 3 but for top 2000 m

FIGURE CAPTIONS

Fig. 1 The domain-averaged temperature and salinity over the North Atlantic (20°N-70°N) upper (200-1000m) (top, *ac*) and lower (1000-5000m) (bottom, *bd*) oceans in T-S space for the control run using the 1860 fixed-year radiative forcings (left, *ab*) and the 20^{th} century histotical run using temporally-varying radiative forcings (right, *cd*). The first 40 years are marked by black dots, and each quarter afterward is marked by cyan, blue, green and red dots respectively.

Fig. 2 Schematic diagram of how the GFDL coupled model (CM2) components – atmosphere, ocean, land and sea-ice interacts each other by exchange fluxes (black arrows). The green arrow denotes the radiative forcings expressed by the atmospheric greenhouse gas and natural aerosol (GHGNA) in the coupled model system, and the dashed means that the GHGNA radiative forcings in assimilation may be set as fixed-year (1860). The red arrows indicate that oceanic observations are allowed to impact all oceanic state variables including the wind stresses at the sea-surface.

Fig. 3 The ensemble spread of the atmosphere (upper) and the ocean (lower) in CM2. Each colored line represents the individual ensemble member's departure from the ensemble mean for time mean temperature. The time mean temperature is computed as the last 10-year time-averaged global mean of a 25-year model ensemble integration initialized from 6 yearly-departed atmospheric states (including land) combing with a common oceanic state (including sea-ice). The model integration uses the 1860 fixed-year GHGNA radiative forcings. The dashed-black lines are the standard deviation of the atmospheric/oceanic temperature, computed by the 6-member ensemble.

Fig. 4 Cartoon of how an ensemble filter updates the distribution for a scalar variable. The upperleft reprsents the prior distribution derived from model ensemble integrations starting from the previous assimilation results. The upperright represents an observational distribution (usually Gaussian). An ensemble filtering process (lower-left) combines the observational and prior distributions to form an updated 'analyzed' distribution (lowerright) realized by the ensemble member states that initialize next ensemble integrations.

Fig. 5 Samples of vertical variations of the 20^{th}-century oceanic observing network. Upper/lower panels are the locations of observational profiles deeper than 500m/1000m in January 1986 (left) and 1991 (right). The background colors show the individual ocean basins that are examined in this study.

Fig. 6 Samples of vertical variations of the 21^{st}-century oceanic observing network (ARGO). Upper/lower panels are the locations of ARGO temperature (left) and salinity (right) profiles deeper than 500m/1000m in January 2005.

Fig. 7 Time series of the averaged oceanic temperature anomalies of top 700 m for individual ocean basins and the world ocean in the 3 free model simulations and 4 ODA experiments (see section 3). One of free model simulation, the GFDL IPCC historical simulation (plotted by black lines) is sampled by the 20^{th}-century or 21^{st}-century oceanic observing network to form 'observations' for ODA, and serves as the target of 4 assimilations: Exp-$IC_cQ_0N_{XBT}$ (dashed-red), Exp-$IC_cQ_tN_{XBT}$ (solid-red), Exp-$IC_fQ_tN_{XBT}$ (dashed-blue) and Exp-$IC_fQ_tN_{ARGO}$ (solid-blue). Other two free model simulations – Ctl-IC_cQ_0 and Ctl-IC_fQ_t – are plotted by the dashed- and solid-green lines as the reference of assimilation evaluation.

Fig. 8 Same as Fig. 7 but for top 2000 m.

Fig. 9 Differences of the time means for 1991-2000 and 1981-1990 of the top 700 m ocean temperature of the truth (a), and the assimilation errors of the difference in Exp-$IC_cQ_0N_{XBT}$ (c), Exp-$IC_cQ_tN_{XBT}$ (d), Exp-$IC_fQ_tN_{XBT}$ (e) and Exp-$IC_fQ_tN_{ARGO}$ (f). The errors of a control case, Ctl-IC_fQ_t, also are exhibted in panel b as a reference for assimilation evaluation. The contour interval is 0.1^oC, the 0-line is omitted and the dashed is negative.

Fig. 10 Same as Fig. 9 but for the top 2000 m ocean and the contour interval is 0.05^oC.

Fig. 11 Same as Fig. 7 but for the salinity.

Fig. 12 Same as Fig. 8 but for the salinity.

Fig. 13 Time series of salinity anomalies averaged at the tropical Pacific (5^oS-5^oN) of top 200 m in the truth (black), 2 control free model runs (dashed-green for Ctl-IC$_c$Q$_0$ and solid-green for Ctl-IC$_f$Q$_t$) and 4 ODA experiments: Exp-IC$_c$Q$_0$N$_{XBT}$ (dashed-red), Exp-IC$_c$Q$_t$N$_{XBT}$ (solid-red), Exp-IC$_f$Q$_t$N$_{XBT}$ (dashed-blue) and Exp-IC$_f$Q$_t$N$_{ARGO}$ (solid-blue).

Fig. 14 Same as Fig. 10 but for the salinity and the contour interval is 0.01 PSU.

Fig. 15 Time series of the assimilated oceanic temperature/salinity (upper/lower) RMS errors, computed in the North Atlantic (20^o-70^oN) of top 2000 m, in Exp-IC$_c$Q$_0$N$_{XBT}$ (dashed-red), Exp-IC$_c$Q$_t$N$_{XBT}$ (solid-red), Exp-IC$_f$Q$_t$N$_{XBT}$ (dashed-blue) and Exp-IC$_f$Q$_t$N$_{ARGO}$ (solid-blue). The corresponding RMS time series for 2 control free model runs (dashed-/solid-green for the Ctl-IC$_c$Q$_0$/Ctl-IC$_f$Q$_t$) are plotted as the reference of assimilation.

Fig. 16 Time series of the averaged oceanic temperature (left) and salinity (right) in the north (20^o-70^oN) Atlantic over the upper (200-1000m, top panels) and lower (1000-5000m, bottom panels) portions of the North Atlantic meridional overturning circulation.

Table 1: The time mean RMS of oceanic temperature errors (^{o}C) over top 700 m during the last 20 years in 2 control and 4 assimilation experiments/the RMS's reduction (%) of assimilation from the case it is compared to (for Exp-IC$_c$Q$_0$N$_{XBT}$ the RMS's reduction is from Ctl-IC$_c$Q$_0$; for Exp-IC$_c$Q$_t$N$_{XBT}$ the reduction is from Exp-IC$_c$Q$_0$N$_{XBT}$; for Exp-IC$_f$Q$_t$N$_{XBT}$ the reduction is from Exp-IC$_c$Q$_t$N$_{XBT}$; for Exp-IC$_f$Q$_t$N$_{ARGO}$ the reduction is from Exp-IC$_f$Q$_t$N$_{XBT}$), the mean errors (10^{-2} ^{o}C) of 4 assimilation and 2 model simulation experiments are listed in parentheses

Basin	Ctl-IC$_c$Q$_0$	Ctl-IC$_f$Q$_t$	Exp-IC$_c$Q$_0$N$_{XBT}$	Exp-IC$_c$Q$_t$N$_{XBT}$	Exp-IC$_f$Q$_t$N$_{XBT}$	Exp-IC$_f$Q$_t$N$_{ARGO}$
SAT	.62(-41)	.60(11)	.22/65(.1)	.21/5(-.1)	.19/10(.2)	.19/0(-.03)
NAT	.84(-25)	1.0(10)	.33/61(-1)	.34/-3(-.2)	.28/18(.2)	.34/-26(-2)
AT	.77(-31)	.91(10)	.30/61(-.6)	.30/0(-.2)	.25/17(.2)	.29/-16(-1)
SIN	.66(9)	.69(-.6)	.38/42(4)	.38/0(4)	.26/32(.6)	.20/30(-.9)
NIN	.69(-41)	.70(24)	.58/16(-2)	.60/-3(-2)	.38/37(1)	.28/33(2)
IN	.68(-4)	.70(6)	.45/34(3)	.45/0(2)	.30/33(.8)	.23/23(-.1)
SPC	.55(-10)	.64(-4)	.17/69(-.4)	.16/6(-.6)	.15/6(-.3)	.19/-26(2)
NPC	.90(-8)	.86(-2)	.22/76(1)	.22/0(1)	.17/23(.1)	.25/-47(2)
PC	.78(-9)	.78(-3)	.21/73(.5)	.20/5(.3)	.16/20(-.1)	.23/-44(2)
SO	.53(-33)	.64(20)	.33/38(-7)	.31/6(-6)	.28/10(2)	.18/36(2)
AO	.53(-17)	.63(19)	.33/38(-4)	.38/-15(-3)	.29/24(2)	.25/14(2)
WO	.71(-19)	.77(7)	.31/56(-2)	.31/0(-1)	.24/23(.7)	.24/0(1)

SAT – South Atlantic Ocean; NAT – North Atlantic Ocean; AT – Atlantic Ocean

SIN – South Indian Ocean; NIN – North Indian Ocean; IN – Indian Ocean

SPC – South Pacific Ocean; SPC – North Pacific Ocean; PC – Pacific Ocean

SO – Southern Ocean; AO – Arctic Ocean; WO – World Ocean

Table 2: Same as Table 1 but for the top 2000 m

Basin	Ctl-IC$_c$Q$_0$	Ctl-IC$_f$Q$_t$	Exp-IC$_c$Q$_0$N$_{XBT}$	Exp-IC$_c$Q$_t$N$_{XBT}$	Exp-IC$_f$Q$_t$N$_{XBT}$	Exp-IC$_f$Q$_t$N$_{ARGO}$
SAT	.31(-19)	.31(10)	.14/55(-.9)	.13/7(-1)	.11/15(2)	.12/-9(-.4)
NAT	.49(-11)	.58(9)	.22/55(-.1)	.22/0(.2)	.19/14(-.3)	.20/-5(.6)
AT	.43(-14)	.50(9)	.19/56(-.4)	.20/-5(-.5)	.17/15(.5)	.17/0(-1)
SIN	.35(7)	.37(2)	.27/23(7)	.27/0(7)	.17/37(3)	.13/24(.2)
NIN	.42(-27)	.44(26)	.53/-26(-18)	.55/-4(-17)	.27/51(-5)	.18/33(-.1)
IN	.37(-2)	.39(8)	.36/3(.3)	.37/-3(.4)	.20/46(.6)	.14/30(.1)
SPC	.26(-6)	.35(8)	.16/39(-1)	.13/19(-1)	.12/8(3)	.10/17(1)
NPC	.41(-.3)	.41(2)	.14/71(2)	.14/0(2)	.10/29(.3)	.12/-20(.5)
PC	.36(-3)	.39(5)	.15/58(.7)	.14/7(.3)	.11/21(1)	.11/0(.7)
SO	.35(-24)	.43(19)	.21/40(-6)	.20/5(-6)	.18/10(3)	.10/44(1)
AO	.37(-12)	.45(21)	.26/30(-2)	.28/-8(-4)	.24/14(5)	.20/17(3)
WO	.38(-11)	.43(10)	.22/42(-2)	.22/0(-2)	.16/27(2)	.13/19(.6)

Table 3: The time mean RMS of oceanic salinity errors (PSU) over top 700 m during the last 20 years in 2 control and 4 assimilation experiments/the RMS's reduction (%) of assimilation from the case it is compared to (for Exp-IC$_c$Q$_0$N$_{XBT}$ the RMS's reduction is from Ctl-IC$_c$Q$_0$; for Exp-IC$_c$Q$_t$N$_{XBT}$ the reduction is from Exp-IC$_c$Q$_0$N$_{XBT}$; for Exp-IC$_f$Q$_t$N$_{XBT}$ the reduction is from Exp-IC$_c$Q$_t$N$_{XBT}$; for Exp-IC$_f$Q$_t$N$_{ARGO}$ the reduction is from Exp-IC$_f$Q$_t$N$_{XBT}$), the mean errors (10^{-2} PSU) of 4 assimilation and 2 model simulation experiments are listed in parentheses

Basin	Ctl-IC$_c$Q$_0$	Ctl-IC$_f$Q$_t$	Exp-IC$_c$Q$_0$N$_{XBT}$	Exp-IC$_c$Q$_t$N$_{XBT}$	Exp-IC$_f$Q$_t$N$_{XBT}$	Exp-IC$_f$Q$_t$N$_{ARGO}$
SAT	.10(-1)	.15(.2)	.08/20(-.4)	.08/0(-.1)	.06/25(.5)	.05/17(-.4)
NAT	.14(-1)	.24(1)	.11/21(-3)	.11/0(-2)	.08/27(2)	.09/-13(-.5)
AT	.13(-1)	.22(.6)	.10/23(-2)	.10/0(-1)	.07/30(1)	.07/0(-.5)
SIN	.15(8)	.15(2)	.14/7(2)	.13/7(3)	.08/38(3)	.05/38(.1)
NIN	.19(-8)	.22(9)	.26/-37(-4)	.26/0(-2)	.17/35(4)	.09/47(2)
IN	.17(4)	.18(3)	.18/-6(.7)	.18/0(2)	.11/39(3)	.06/46(.7)
SPC	.10(2)	.14(-3)	.06/40(.2)	.06/0(2)	.05/17(-1)	.04/20(-.3)
NPC	.14(5)	.16(-.7)	.08/43(4)	.08/0(4)	.05/38(-.8)	.04/20(.05)
PC	.13(4)	.15(-2)	.07/46(2)	.07/0(3)	.05/29(-1)	.04/20(-.1)
SO	.08(3)	.10(-.8)	.07/13(3)	.07/0(3)	.05/29(1)	.03/40(.1)
AO	.12(3)	.17(-.6)	.09/25(4)	.12/-33(3)	.07/42(2)	.06/14(-1)
WO	.13(3)	.16(-.4)	.10/23(1)	.10/0(2)	.07/30(.5)	.05/29(-.1)

Table 4: Same as Table 3 but for the upper 2000 m of the ocean

Basin	Ctl-IC$_c$Q$_0$	Ctl-IC$_f$Q$_t$	Exp-IC$_c$Q$_0$N$_{XBT}$	Exp-IC$_c$Q$_t$N$_{XBT}$	Exp-IC$_f$Q$_t$N$_{XBT}$	Exp-IC$_f$Q$_t$N$_{ARGO}$
SAT	.05(-1)	.07(.8)	.05/0(-1)	.05/0(-1)	.04/20(-1)	.03/25(-.1)
NAT	.07(-.5)	.12(1)	.06/14(-1)	.06/0(-1)	.04/33(.5)	.05/-25(-.05)
AT	.07(-.8)	.10(1)	.06/29(-1)	.06/0(-1)	.04/33(.7)	.07/-75(-.02)
SIN	.07(3)	.07(.6)	.09/-29(1)	.08/11(2)	.05/38(2)	.03/40(.4)
NIN	.11(-6)	.18(7)	.18/-64(-7)	.18/0(-6)	.09/50(1)	.05/44(.8)
IN	.09(.7)	.09(2)	.12/-33(-1)	.12/0(-.4)	.06/50(2)	.04/33(.5)
SPC	.05(-.1)	.06(-.4)	.04/20(-2)	.04/0(-.8)	.03/25(-.4)	.02/33(.1)
NPC	.06(2)	.07(-1)	.05/17(1)	.05/0(1)	.03/40(-1)	.02/33(-.2)
PC	.06(1)	.07(-1)	.05/17(.1)	.04/20(.5)	.03/25(-.7)	.02/33(-.04)
SO	.05(-.3)	.06(.8)	.05/0(-1)	.05/0(-1)	.03/20(1)	.02/33(.1)
AO	.06(1)	.08(1)	.05/17(1)	.06/-20(.6)	.04/33(.6)	.03/25(-1)
WO	.06(.3)	.08(.3)	.07/-17(-.5)	.07/0(-.3)	.04/43(.3)	.03/25(.03)

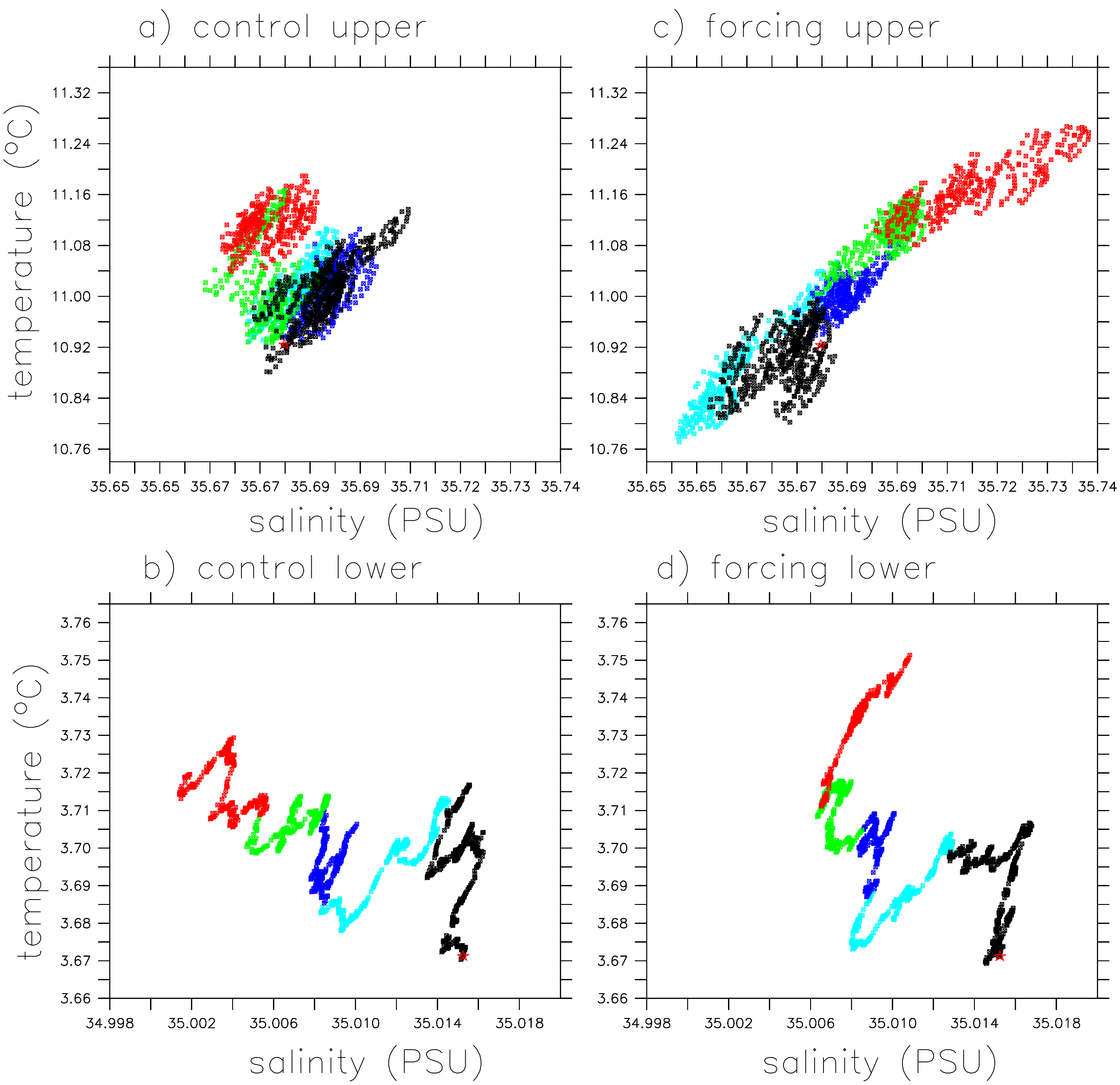

Figure 1: The domain-averaged temperature and salinity over the North Atlantic (20°N-70°N) upper (200-1000m) (top, *ac*) and lower (1000-5000m) (bottom, *bd*) oceans in T-S space for the control run using the 1860 fixed-year radiative forcings (left, *ab*) and the 20th century histotical run using temporally-varying radiative forcings (right, *cd*). The first 40 years are marked by black dots, and each quarter afterward is marked by cyan, blue, green and red dots respectively.

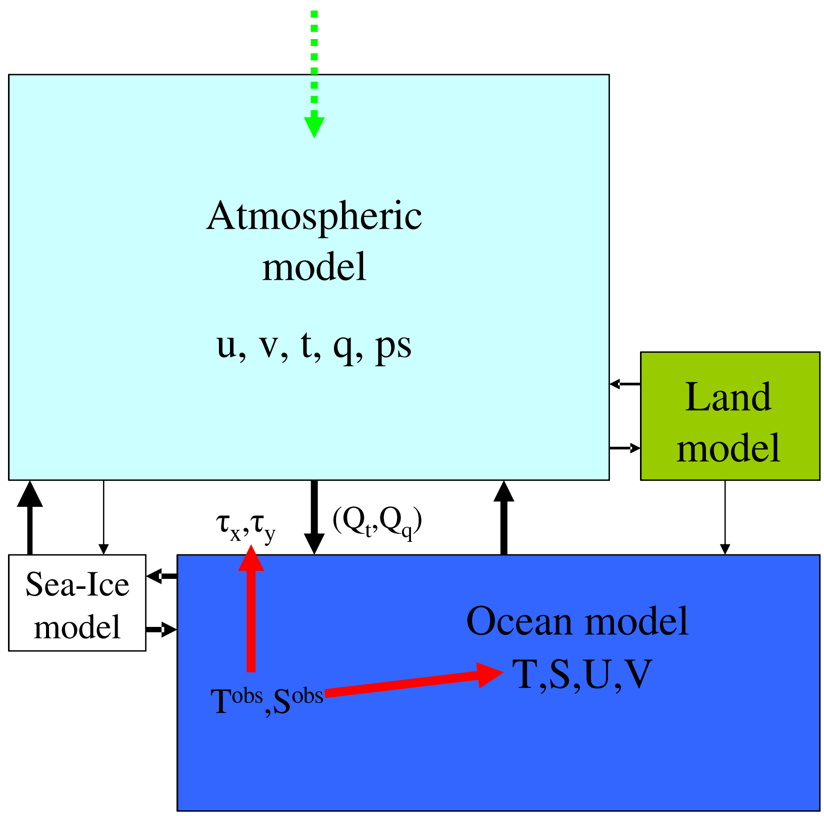

Figure 2: Schematic diagram of how the GFDL coupled model (CM2) components – atmosphere, ocean, land and sea-ice interacts each other by exchange fluxes (black arrows). The green arrow denotes the radiative forcings expressed by the atmospheric greenhouse gas and natural aerosol (GHGNA) in the coupled model system, and the dashed means that the GHGNA radiative forcings in assimilation may be set as fixed-year (1860). The red arrows indicate that oceanic observations are allowed to impact all oceanic state variables including the wind stresses at the sea-surface.

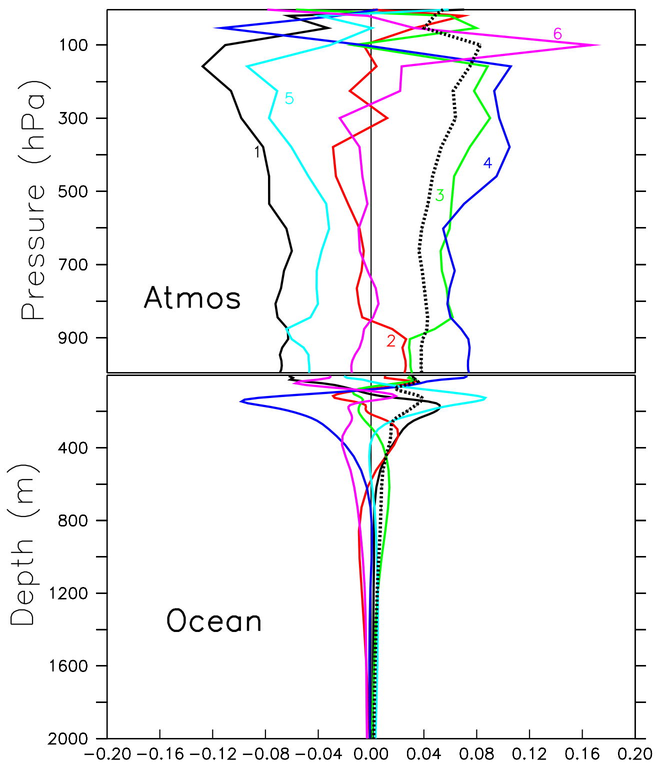

Figure 3: The ensemble spread of the atmosphere (upper) and the ocean (lower) in CM2. Each colored line represents the individual ensemble member's departure from the ensemble mean for time mean temperature. The time mean temperature is computed as the last 10-year time-averaged global mean of a 25-year model ensemble integration initialized from 6 yearly-departed atmospheric states (including land) combing with a common oceanic state (including sea-ice). The model integration uses the 1860 fixed-year GHGNA radiative forcings. The dashed-black lines are the standard deviation of the atmospheric/oceanic temperature, computed by the 6-member ensemble.

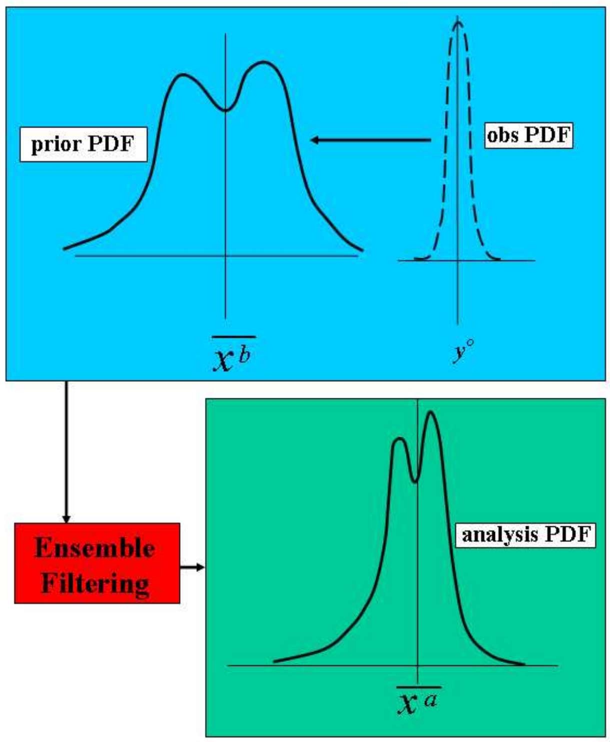

Figure 4: Cartoon of how an ensemble filter updates the distribution for a scalar variable. The upperleft reprsents the prior distribution derived from model ensemble integrations starting from the previous assimilation results. The upperright represents an observational distribution (usually Gaussian). An ensemble filtering process (lowerleft) combines the observational and prior distributions to form an updated 'analyzed' distribution (lowerright) realized by the ensemble member states that initialize next ensemble integrations.

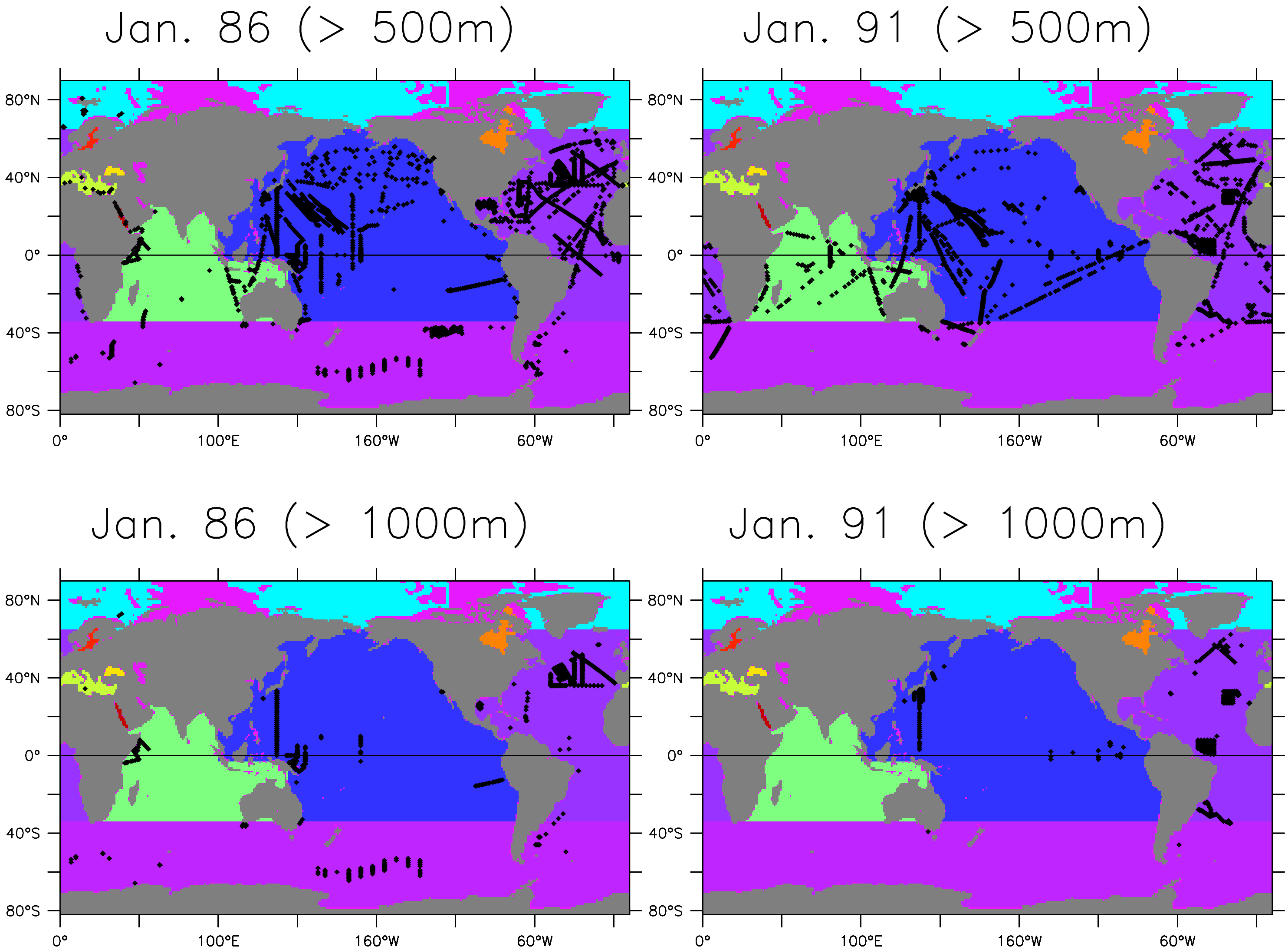

Figure 5: Samples of vertical variations of the 20^{th}-century oceanic observing network. Upper/lower panels are the locations of observational profiles deeper than 500m/1000m in January 1986 (left) and 1991 (right). The background colors show the individual ocean basins that are examined in this study.

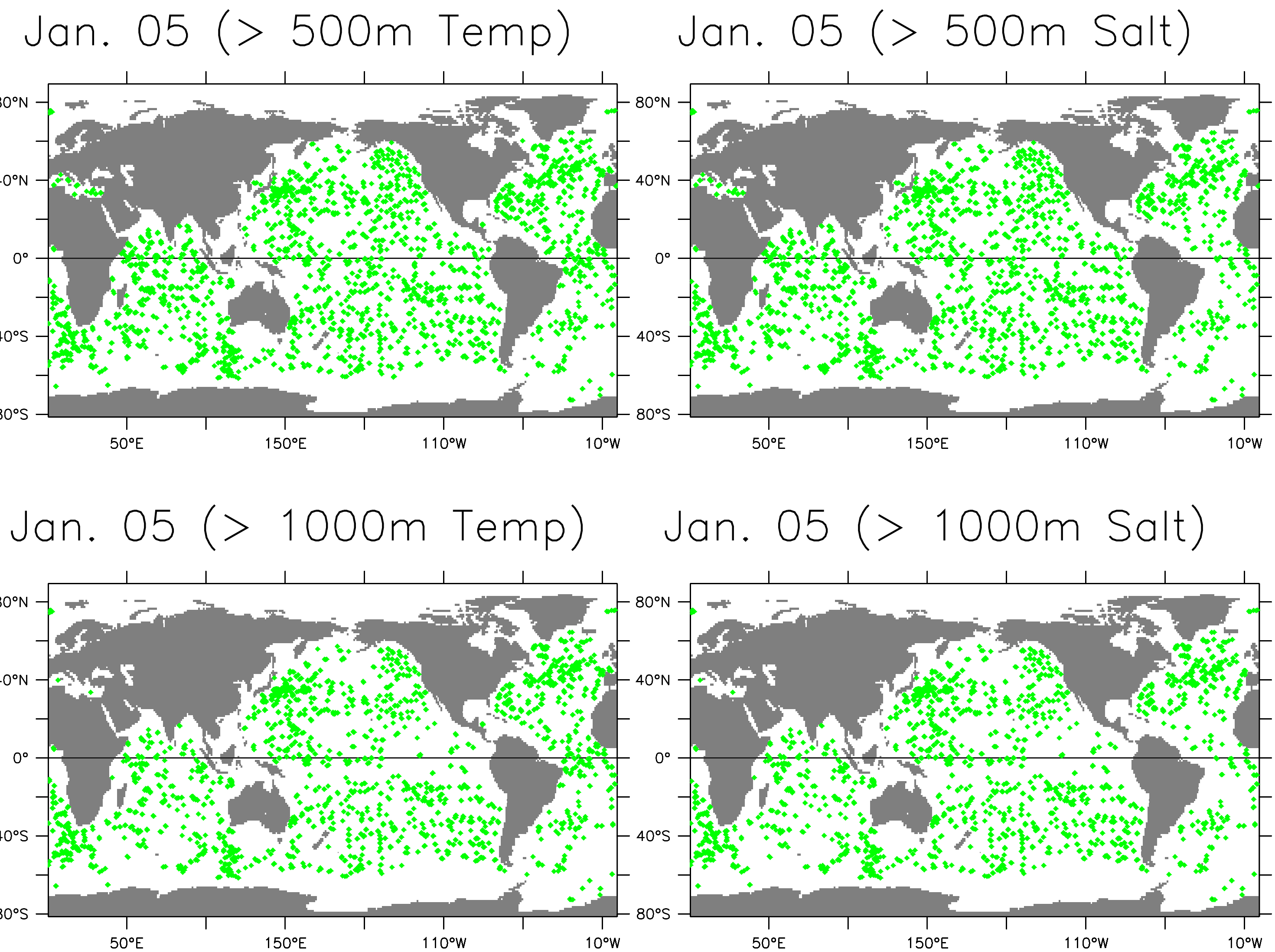

Figure 6: Samples of vertical variations of the 21^{st}-century oceanic observing network (ARGO). Upper/lower panels are the locations of ARGO temperature (left) and salinity (right) profiles deeper than 500m/1000m in January 2005.

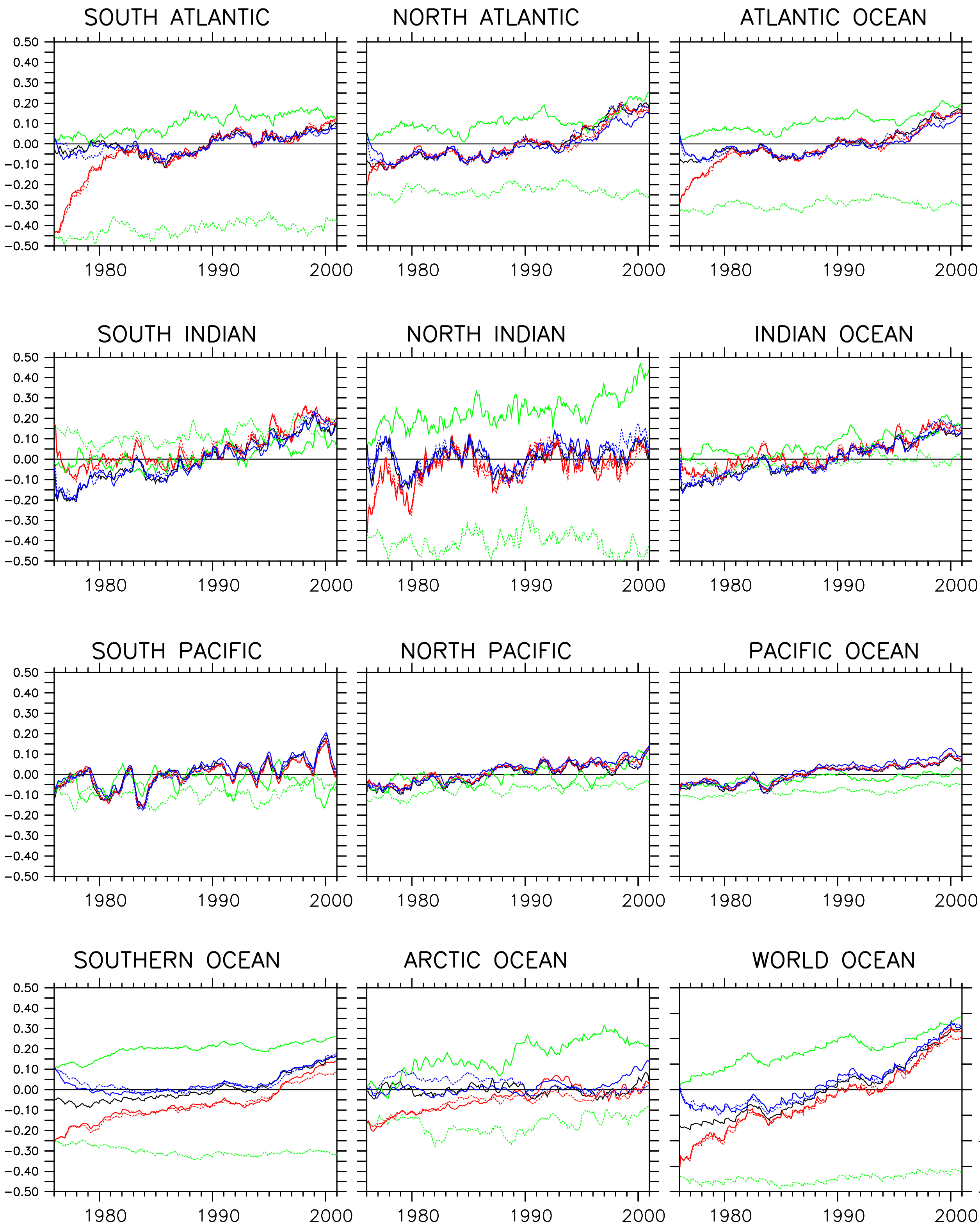

Figure 7: Time series of the averaged oceanic temperature anomalies of top 700 m for individual ocean basins and the world ocean in the 3 free model simulations and 4 ODA experiments (see section 3). One of free model simulation, the GFDL IPCC historical simulation (plotted by black lines) is sampled by the 20^{th}-century or 21^{st}-century oceanic observing network to form 'observations' for ODA, and serves as the target of 4 assimilations: Exp-$IC_cQ_0N_{XBT}$ (dashed-red), Exp-$IC_cQ_tN_{XBT}$ (solid-red), Exp-$IC_fQ_tN_{XBT}$ (dashed-blue) and Exp-$IC_fQ_tN_{ARGO}$ (solid-blue). Other two free model simulations – Ctl-IC_cQ_0 and Ctl-IC_fQ_t – are plotted by the dashed- and solid-green lines as the reference of assimilation evaluation.

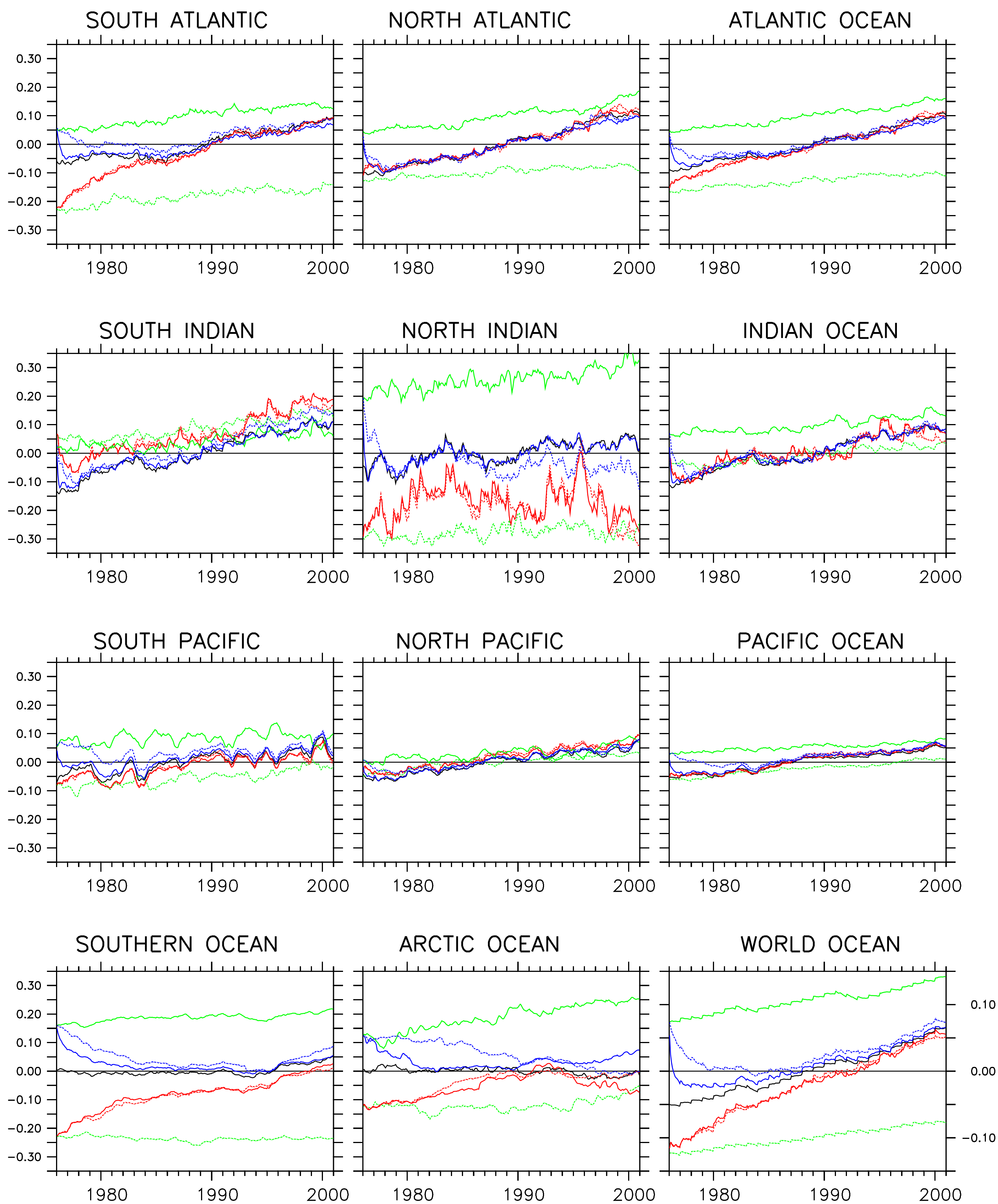

Figure 8: Same as Fig. 7 but for top 2000 m.

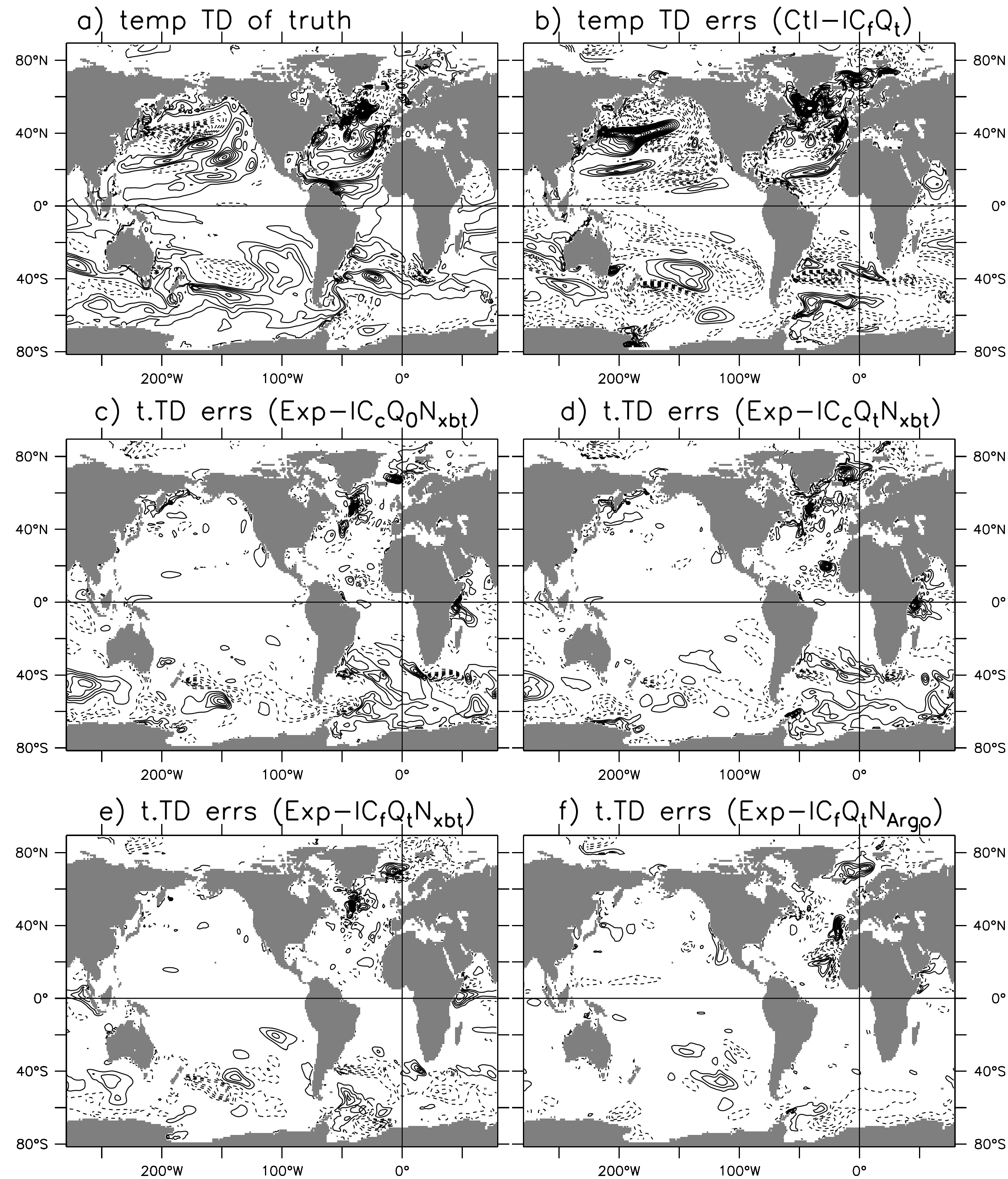

Figure 9: Differences of the time means for 1991-2000 and 1981-1990 of the top 700 m ocean temperature of the truth (a), and the assimilation errors of the difference in Exp-IC$_c$Q$_0$N$_{XBT}$ (c), Exp-IC$_c$Q$_t$N$_{XBT}$ (d), Exp-IC$_f$Q$_t$N$_{XBT}$ (e) and Exp-IC$_f$Q$_t$N$_{ARGO}$ (f). The errors of a control case, Ctl-IC$_f$Q$_t$, also are exhibted in panel b as a reference for assimilation evaluation. The contour interval is 0.1^{o}C, the 0-line is omitted and the dashed is negative.

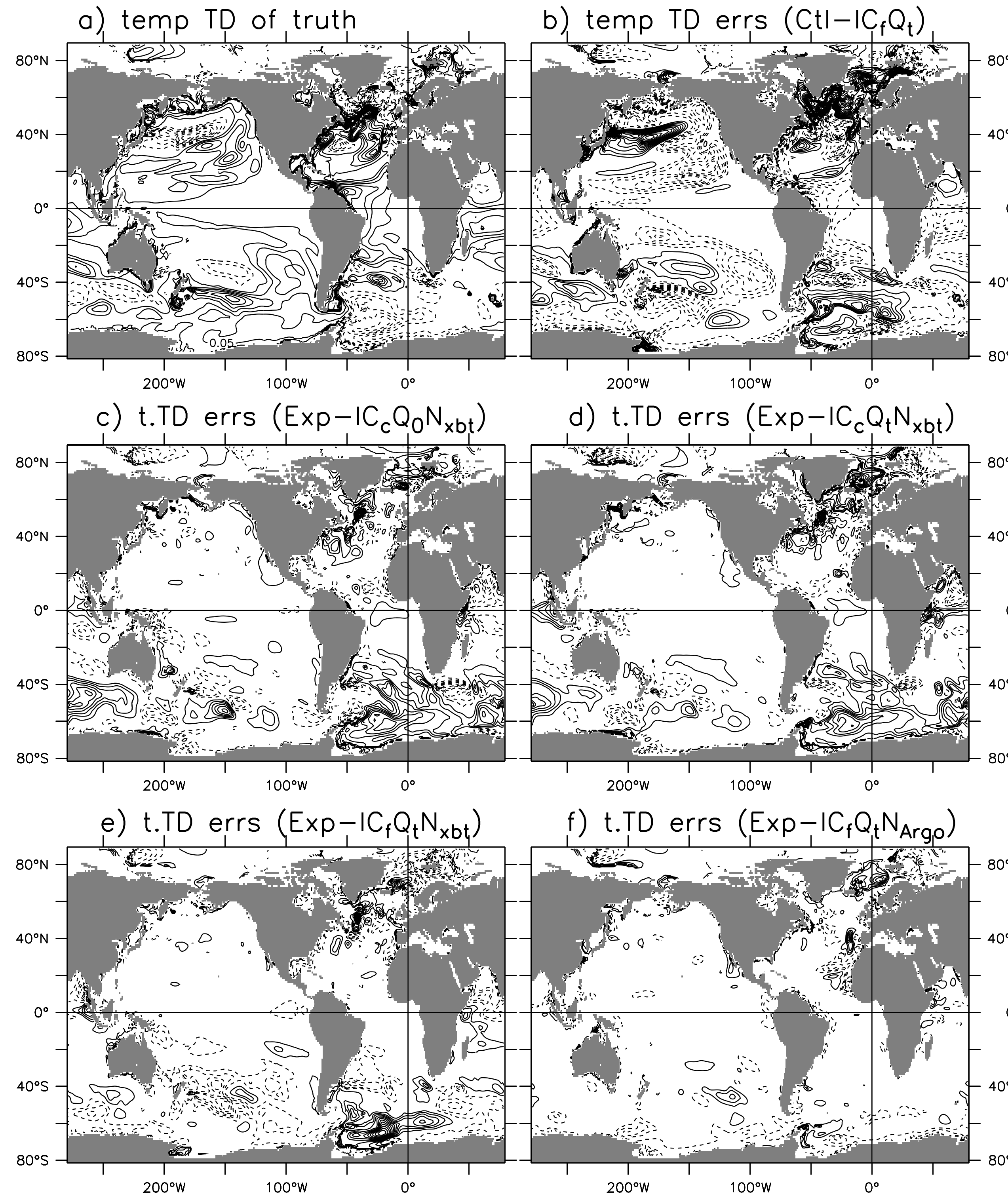

Figure 10: Same as Fig. 9 but for the top 2000 m ocean and the contour interval is 0.05^oC.

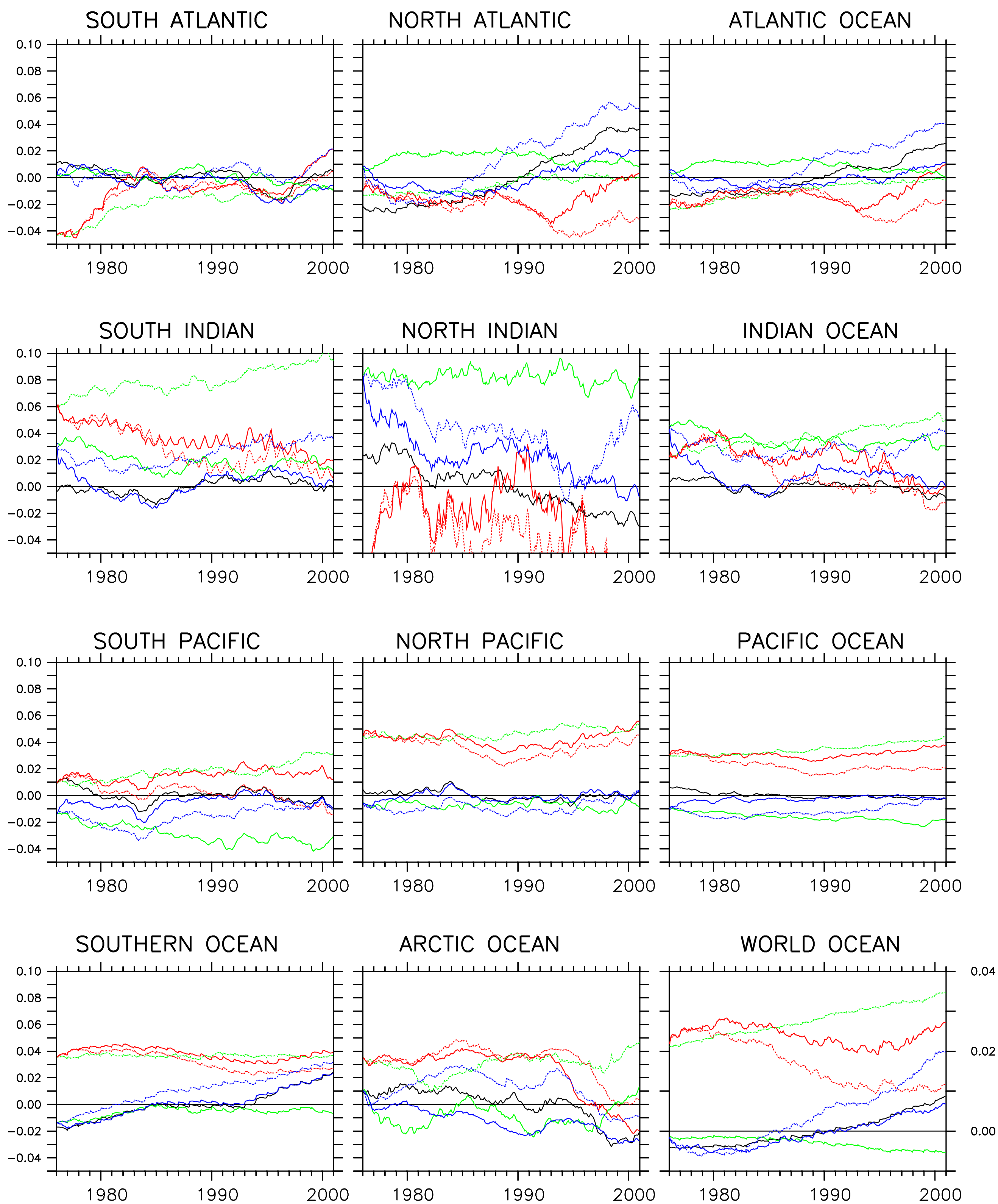

Figure 11: Same as Fig. 7 but for the salinity.

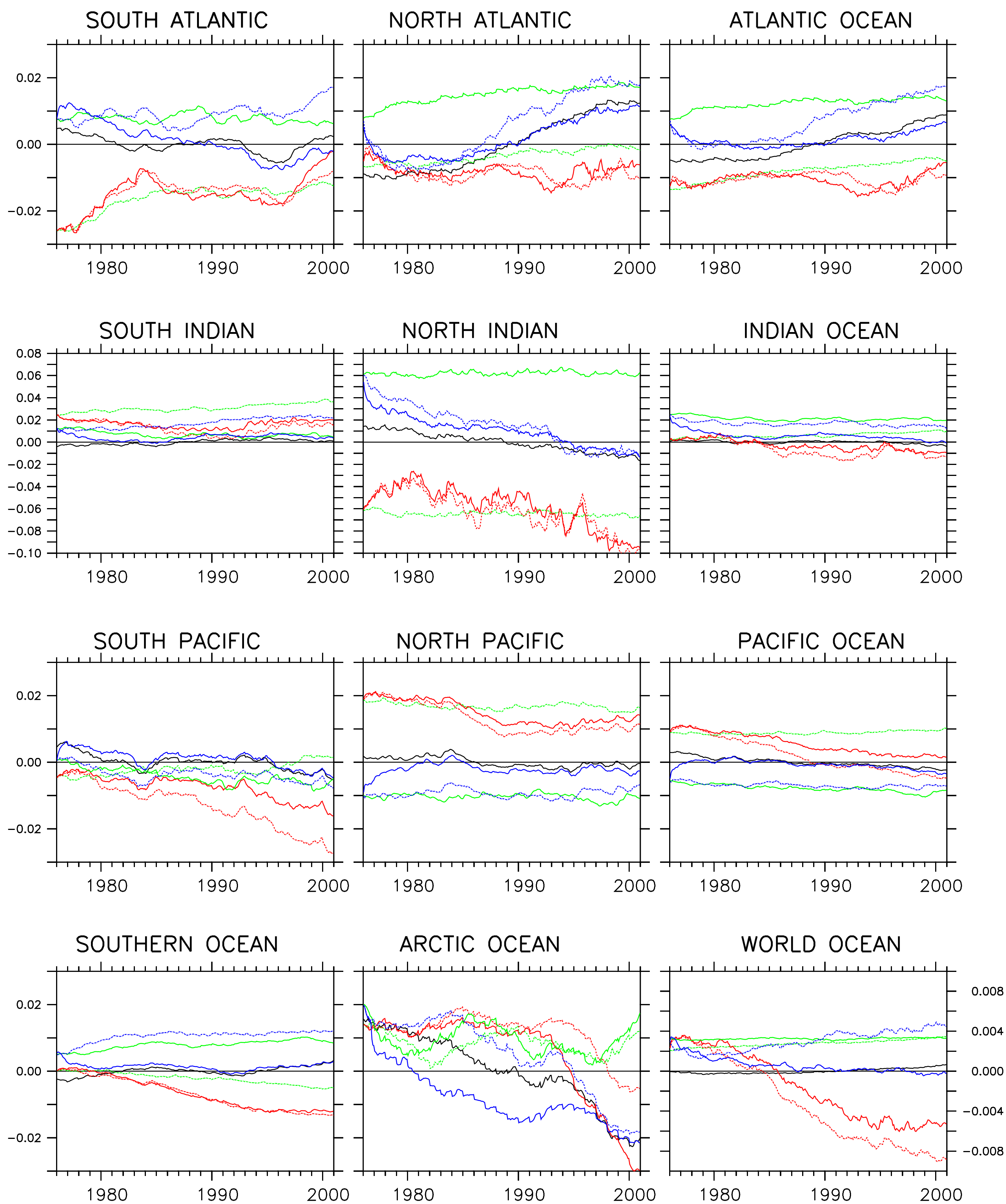

Figure 12: Same as Fig. 8 but for the salinity.

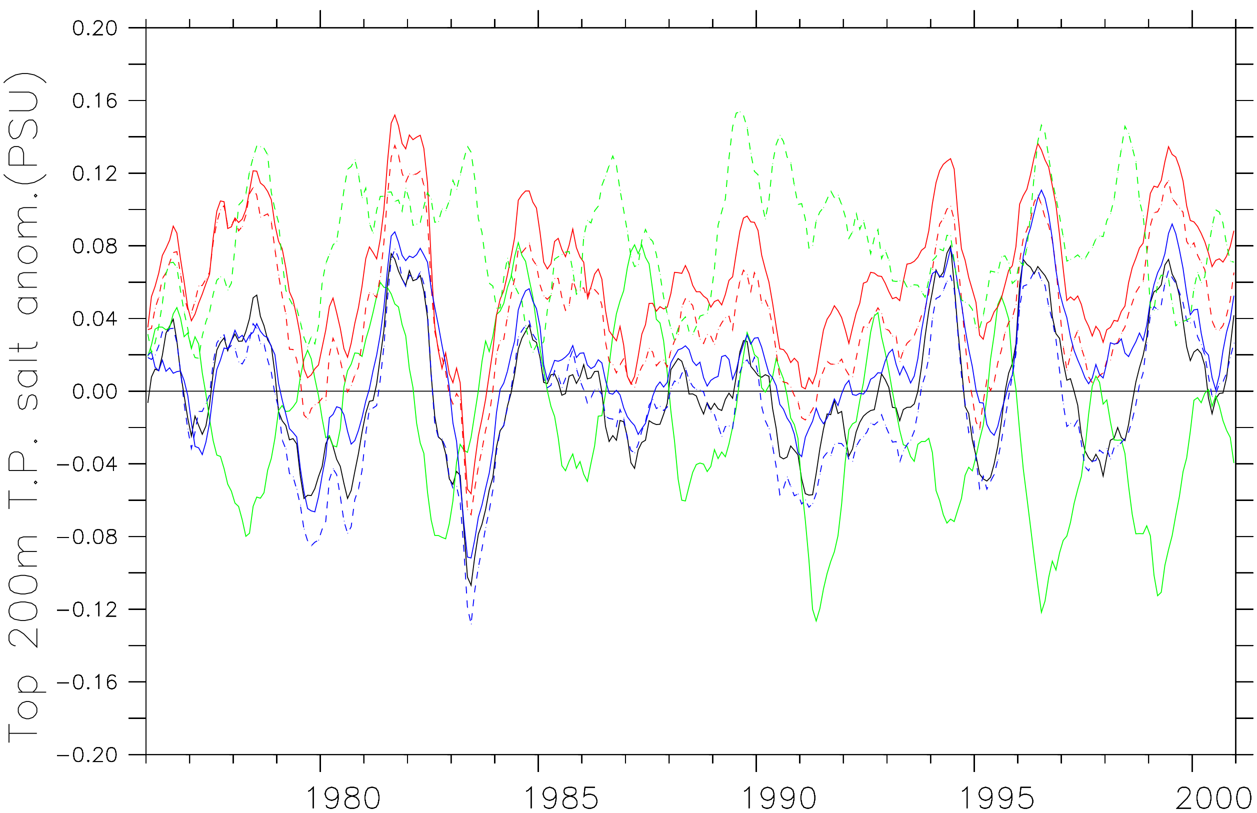

Figure 13: Time series of salinity anomalies averaged at the tropical Pacific (5^oS-5^oN) of top 200 m in the truth (black), 2 control free model runs (dashed-green for Ctl-IC$_c$Q$_0$ and solid-green for Ctl-IC$_f$Q$_t$) and 4 ODA experiments: Exp-IC$_c$Q$_0$N$_{XBT}$ (dashed-red), Exp-IC$_c$Q$_t$N$_{XBT}$ (solid-red), Exp-IC$_c$Q$_0$N$_{XBT}$ (dashed-blue) and Exp-IC$_f$Q$_t$N$_{ARGO}$ (solid-blue).

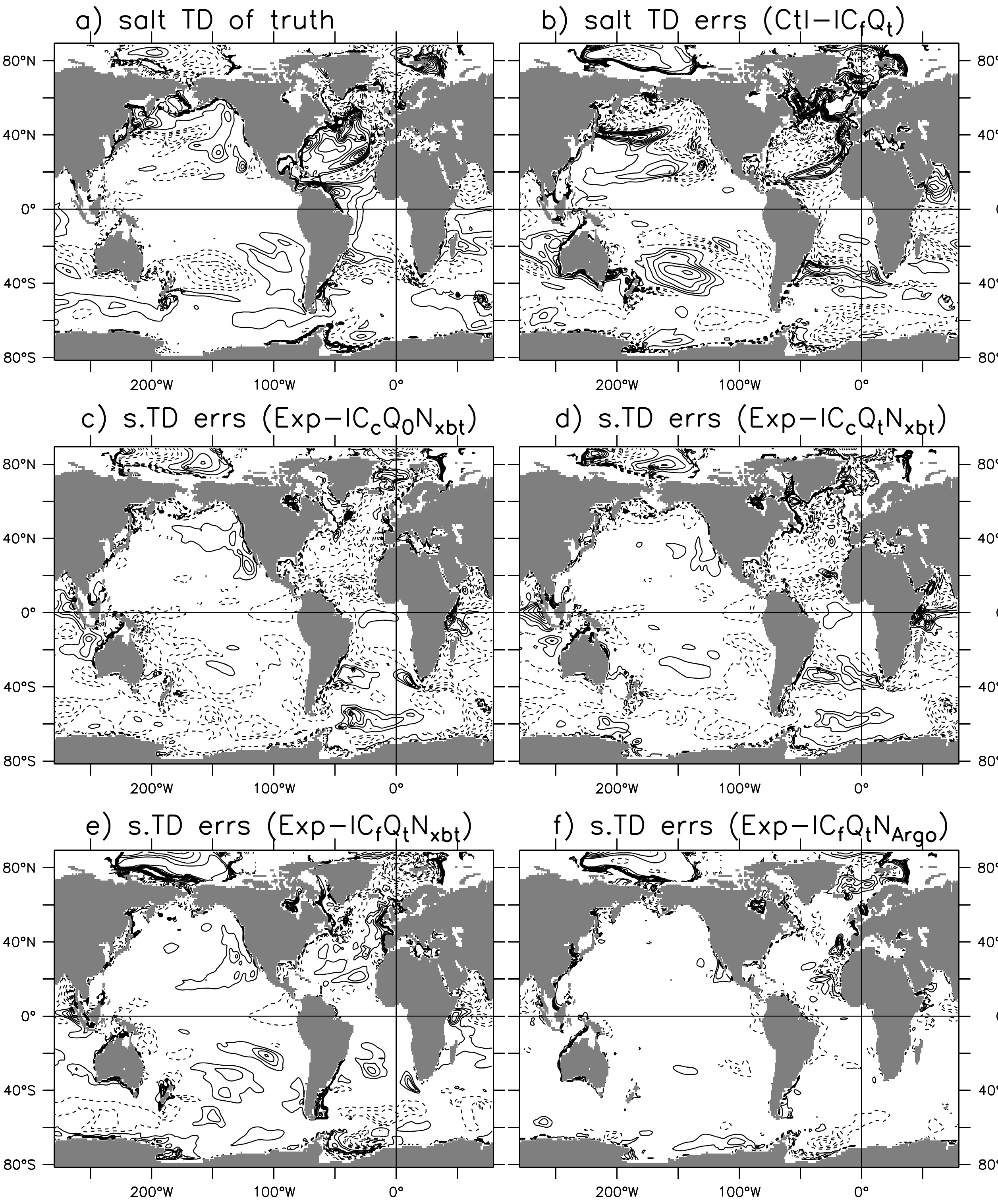

Figure 14: Same as Fig. 10 but for the salinity and the contour interval is 0.01 PSU.

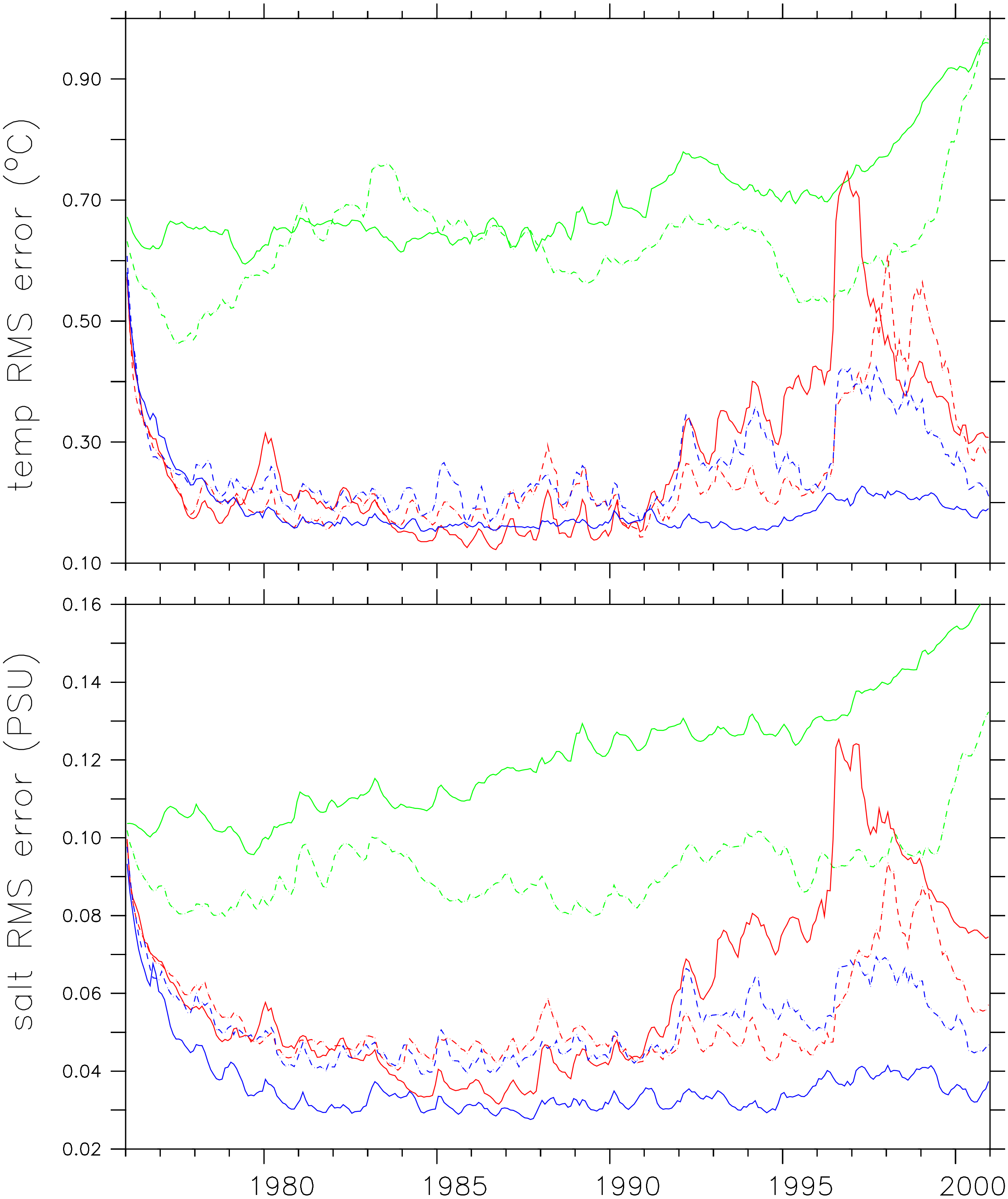

Figure 15: Time series of the assimilated oceanic temperature/salinity (upper/lower) RMS errors, computed in the North Atlantic (20^o-70^oN) of top 2000 m, in Exp-IC$_c$Q$_0$N$_{XBT}$ (dashed-red), Exp-IC$_c$Q$_t$N$_{XBT}$ (solid-red), Exp-IC$_f$Q$_t$N$_{XBT}$ (dashed-blue) and Exp-IC$_f$Q$_t$N$_{ARGO}$ (solid-blue). The corresponding RMS time series for 2 control free model runs (dashed-/solid-green for the Ctl-IC$_c$Q$_0$/Ctl-IC$_f$Q$_t$) are plotted as the reference of assimilation.

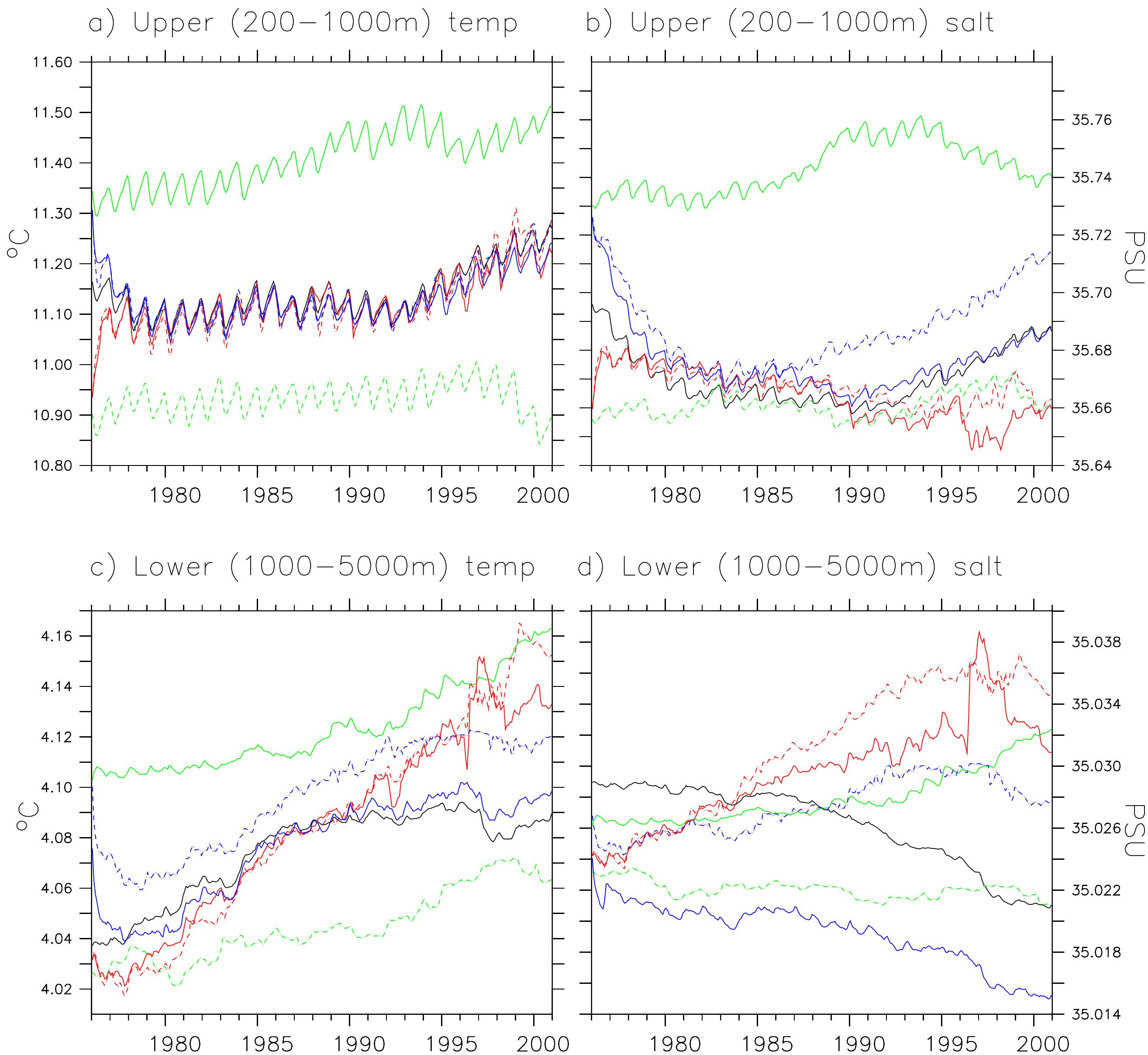

Figure 16: Time series of the averaged oceanic temperature (left) and salinity (right) in the north (20^o-70^oN) Atlantic over the upper (200-1000m, top panels) and lower (1000-5000m, bottom panels) portions of the North Atlantic meridional overturning circulation.